

**Characterizations and Stress Corrosion Cracking Evaluations of Alloy 600
CRDM Nozzle Heats from the Davis Besse Nuclear Power Plant**

S. M. Bruemmer, M. J. Olszta, D. K. Schreiber, N. R. Overman and M. B. Toloczko
Pacific Northwest National Laboratory

Office of Nuclear Regulatory Research

Project JCN – N6925

Primary Water Stress Corrosion Cracking
of High-Chromium, Nickel-Base Alloys

NRC Project Manager: Darrell Dunn

Executive Summary

The original Davis Besse reactor pressure vessel (RPV) head experienced intergranular stress corrosion cracking (IGSCC) of several alloy 600 control rod drive mechanism (CRDM) nozzles. Of particular note was the SCC of nozzle #3 and its alloy 182 J-groove weld to the RPV head that led to boric acid corrosion of the head. This severe damage was identified in 2002 after ~16 effective full power years (EFPY) of operation and led to vessel head replacement using one from the cancelled Midland plant. Surprisingly, SCC was again identified in the alloy 600 replacement head CRDM nozzles after only ~5.5 EFPY in early 2010. Because through-wall failures in both the original and the first replacement reactor pressure vessel head occurred in a relatively short period of time compared to previous operating experience, testing has been conducted to confirm SCC growth rates in these heats. Microstructural characterizations were also performed in an attempt to better understand alloy 600 material conditions promoting high IGSCC susceptibility in PWR primary water service.

Two heats of alloy 600 CRDM tubing, one from the original and one from the replacement Davis Besse RPV heads were obtained for SCC testing. Characterization of these materials revealed that the CRDM material from nozzle #1 of the original head (heat M3935) had a very large grain size of 150-400 μm and a high density of semi-continuous grain boundary carbides. The material from nozzle #4 of the replacement head (heat M7929) had a relatively fine grain size ranging from ~10-25 μm in diameter, and carbides were primarily dispersed throughout the material on grain boundaries. High-resolution measurements revealed that both nozzle materials had high levels of grain boundary boron segregation.

SCC testing was performed at 325°C on two 0.5T CT specimens cut from the original head nozzle (heat M3935) and on two 0.25T CT specimens cut from the replacement head nozzle (heat 7929). Both materials readily transitioned to 100% intergranular cracking and exhibited moderate-to-high SCC growth rates consistent with known behavior for alloy 600. Crack growth rates trended along the 75% bounding line of the MRP-55 alloy 600 curve for the small grained replacement head CRDM heat 7929 material where in-service cracking was observed after only ~5.5 years, while the CRDM heat M3935 material from the original head that was in service for ~16 years trended closer to the 50% bounding line.

SCC growth rates measured for the replacement head heat 7929 nozzle are similar to that reported by ANL for testing on the same nozzle. The response measured by PNNL for nozzle #1 from the original head is distinctly different than that reported by ANL for nozzle #3 from the original head even though both nozzles are identified as heat M3935. ANL's reported crack growth rates are ~10x higher when accounting for expected differences in the corrosion potential (dissolved hydrogen concentrations) on the SCC propagation rate. A difference in grain size for nozzle #3 tested by ANL and nozzle #1 tested by PNNL suggest that microstructural differences may be responsible for the difference in SCC susceptibility. The effect of temperature on constant K crack growth was assessed on the replacement head heat 7929 material specimens with the activation energy found to be ~128 kJ/mol. This value is consistent with that measured by ANL. The effect of stress intensity was also assessed and found to reasonably well follow the MRP-55 trend line for the range of K values studied.

Introduction

The original Davis Besse reactor pressure vessel (RPV) head experienced intergranular stress corrosion cracking (IGSCC) of several alloy 600, control rod drive mechanism (CRDM) nozzles. Of particular note was the SCC of nozzle #3 and its alloy 182 J-groove weld to the RPV head that led to boric acid corrosion of the head. This severe damage was identified in 2002 after ~16 effective full power years (EFPY) of operation and led to vessel head replacement using one from the cancelled Midland plant. Surprisingly, SCC was again identified in the alloy 600 replacement head CRDM nozzles after only ~5.5 EFPY in early 2010. Because through-wall failures in both the original and the first replacement reactor pressure vessel head occurred in a relatively short period of time compared to previous operating experience, testing has been conducted to confirm SCC growth rates in these heats. Microstructural characterizations were also performed in an attempt to better understand alloy 600 material conditions promoting high IGSCC susceptibility in PWR primary water service.

Materials

The alloy 600 CRDM nozzle heats (M3935 - original head and M7929 - replacement head) showing high SCC susceptibility in PWR primary water service were both produced by Babcock & Wilcox Tubular Products Division. Reported bulk compositions for the heats are given in Table 1 along with new glow discharge mass spectroscopy (GDMS) measurements of B concentrations. It is important to note that these are very high levels of B in comparison to other alloy 600 materials we have examined. Limited information was available concerning the processing and heat treatments given to these alloy 600 tubes. Both were in the mill-annealed (MA) condition and the heat M3935 material was reported to have a final MA temperature of 871 to 927°C. Mill specs did indicate that the M3935 heat had a slightly higher yield strength (334 MPa) than the heat M7929 (296 MPa).

In addition to the Davis Besse materials, a section of CRDM nozzle 31 and its alloy 182 weld removed from the North Anna 2 RPV head was available at PNNL for characterization (and possible future SCC testing). Destructive exams were performed in 2007 documenting extensive stress corrosion cracks in the alloy 182 weld that extended into the alloy 600 nozzle. Multiple sectioning was employed to obtain a detailed map of the cracking morphology and then was directly compared to non-destructive evaluations. Selected microstructural exams were also conducted on this alloy 600 service material and are described here for comparison to the Davis Besse heats. No information was available on the North Anna 2 nozzle 31 heat at this time. It is identified as NA2-N31 in this report.

Table 1. Alloy 600 composition (wt% unless noted)

RPV Head	Heat	Ni	Cr	Fe	Mn	C	Si	Cu	P	S	B, appm
Original	M3935	77.9	15.6	6.3	0.27	0.028	0.37	0.01	0.004	0.0022	69
Replacement	M7929	75.3	16.1	7.2	0.26	0.03	0.45	0.01	N/A	0.003	77

The first alloy 600 materials received for testing were from nozzle #4 of the replacement head (heat M7929). The Nuclear Regulatory Commission (NRC) obtained a section of this nozzle, had it decontaminated and compact tension (CT) specimens were machined. PNNL was given two 1/4T CT specimens (identified as DB-1 and DB-2) from locations within the CRDM tube wall as illustrated in Figure 1. Both specimens were in the circumferential-radial (CR) orientation with DB-1 sampling a region closer to the tube OD and DB-2 closer to the tube ID. The remaining specimens were tested at Argonne National Laboratory (ANL).

A section of CRDM nozzle #1 from the original Davis Besse RPV head was in storage at PNNL. This nozzle is made from alloy 600 heat M3935 and is the same heat of alloy 600 used to make nozzle #3 from the original head that was tested by ANL and reported in NUREG/CR-6921. A portion of nozzle #1 was sent to Babcock & Wilcox Technical Services (BWTS) for decontamination and sectioning. The first CT specimen blanks were cut from the 90 degree and 270 degree locations on the 2.5" long section of the nozzle as shown in Figure 2 (items labeled A) and were found to be freely releasable. These blanks were shipped to PNNL and machined into 0.5T CT specimens. BWTS was able to machine out the remaining blanks as shown in Figure 2 and Figure 3 that will be used for both SCC crack-growth and initiation testing as well as additional tensile specimen blanks.

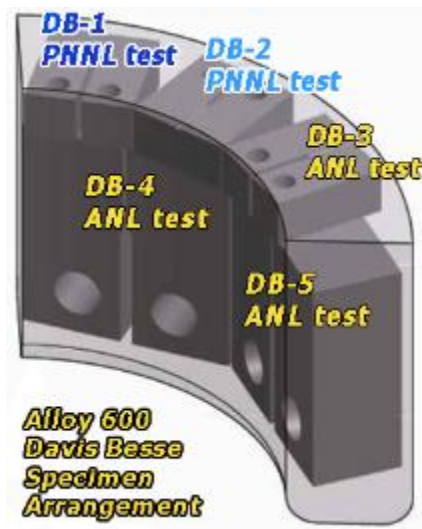


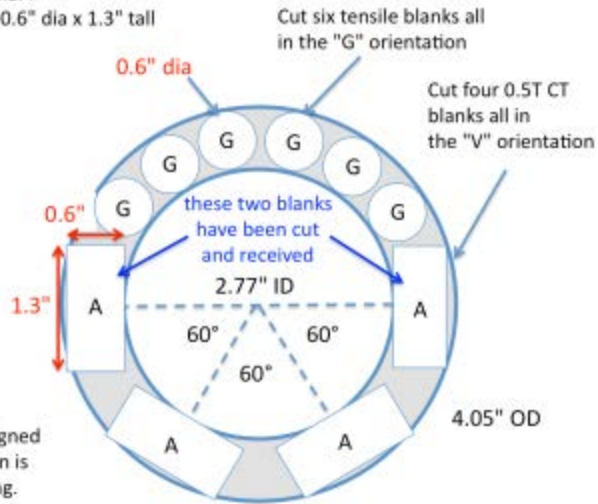
Figure 1. Orientation of DB-1 and DB-2 CT specimens relative to the alloy 600 CRDM tube from which they were machined. Original graphic was created by BWTS.

DB Nozzle #1 - 2.5" tall piece – blank cutting plan
page 1 of 2

Step 1: Cut the 2.5" tall piece into a 1.4" tall slice and a remaining ~1" tall slice.
Step 2: Cut all blanks on this page from the 1.4" tall slice.

- 0.5T CT blank dimensions: 0.6"x1.3"x1.4"
- guillotine tensile blank dimensions: 0.6" dia x 1.3" tall
tolerance: -0.00", +0.05"

G = guillotine orientation
A = axial split orientation



General note: specimens are to be aligned so that the center line of the specimen is coincident with a radius line of the ring.

Figure 2. Cut plan for t0.5T CT specimen and tensile specimen blanks for a 1.4 inch tall slice of nozzle #1 of the original Davis Besse RPV head.

DB Nozzle #1 - 2.5" tall piece – blank cutting plan
page 2 of 2

Step 3: Cut all blanks on this page from the ~1" tall slice.
- split tensile blank dimensions: 0.6" wide x height of ring x 1.25" long
tolerance: -0.00", +0.05"

S = split tensile

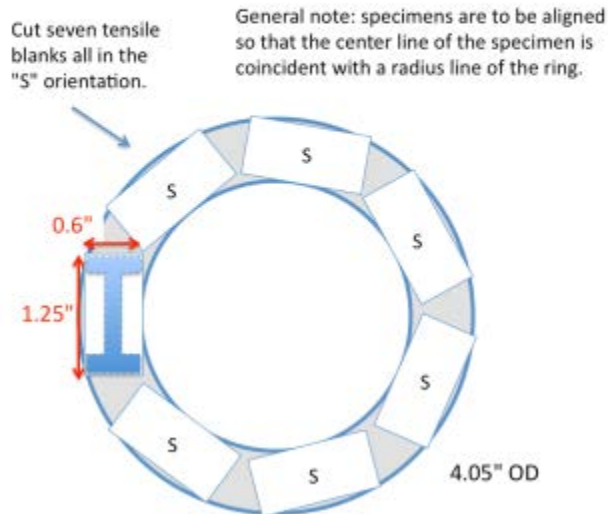


Figure 3. Cut plan for a ~1" tall slice of nozzle #1 from the original Davis Besse RPV head.

Materials Characterizations

General microstructural examinations have been completed and are summarized here on the alloy 600 materials from the replacement (CRDM nozzle #4, heat M7929) and original (CRDM nozzle #1, heat M3935) Davis Besse RPV heads. In addition, selected characterizations were also performed on CRDM nozzle #31 from the North Anna 2 RPV head.

Scanning Electron Microscopy (SEM) Microstructural Characterizations on Alloy 600 Heats

General microstructures are presented for all three heats in Figures 4-7. Low magnification images show the grain size and morphology while higher magnification images reveal the overall carbide density and location. The microstructural data (grain size, approximate carbide density and carbide location) from each material is summarized in Table 2.

Microstructures from CRDM nozzle heat M7929 (replacement head, nozzle #4) are shown in Figure 4, while microstructure for M3935 (original head, nozzle #1) are given in Figures 5 and 6. These two CRDM nozzles came from RPV heads produced by the same manufacturer, so it is surprising that they exhibit strikingly different microstructures. The large difference in grain size is immediately apparent between these two alloy 600 materials reported to be in the mill-annealed condition. The grains range in diameter from ~10-25 μm for M7929, whereas they from ~150-400 μm in diameter for M3935. Most carbides in M7929 were determined to transgranular (TG), while the carbides in M3935 are nearly all IG and spaced ~500 nm apart. The TG carbides in M7929 were not randomly dispersed throughout the grains, but typical associated with ghost or prior grain boundaries. This suggests that the final heat treatment for M7929 was not at sufficiently high temperature to dissolve the pre-existing carbides, but did cause grain boundary migration and create a new grain structure. In contrast, the M3935 material had an extremely large grain size, indicating that it was annealed at a temperature sufficient to dissolve most, if not all, the carbides and promote significant grain growth. Grain boundaries exhibited a semi-continuous distribution of carbides consistent with a slower cooling rate from the annealing temperature enabling precipitation to occur. At higher magnification using a 3 kV accelerating voltage (Figure 6), a population of elongated white particles was observed on many grain boundaries. These particles were determined to be Ni borides by atom probe tomography (APT) and are probably Ni_{23}B_6 forming adjacent to the Cr_7C_3 carbides.

The microstructure for the North Anna 2 alloy 600 CRDM nozzle 31 material (identified as NA2-N31) is illustrated in Figure 7. The sample had an equiaxed grain microstructure with grains ~50-70 μm in size. There was a high density of TG carbides along ghost grain boundaries similar to that for M7929 and only isolated IG carbides.

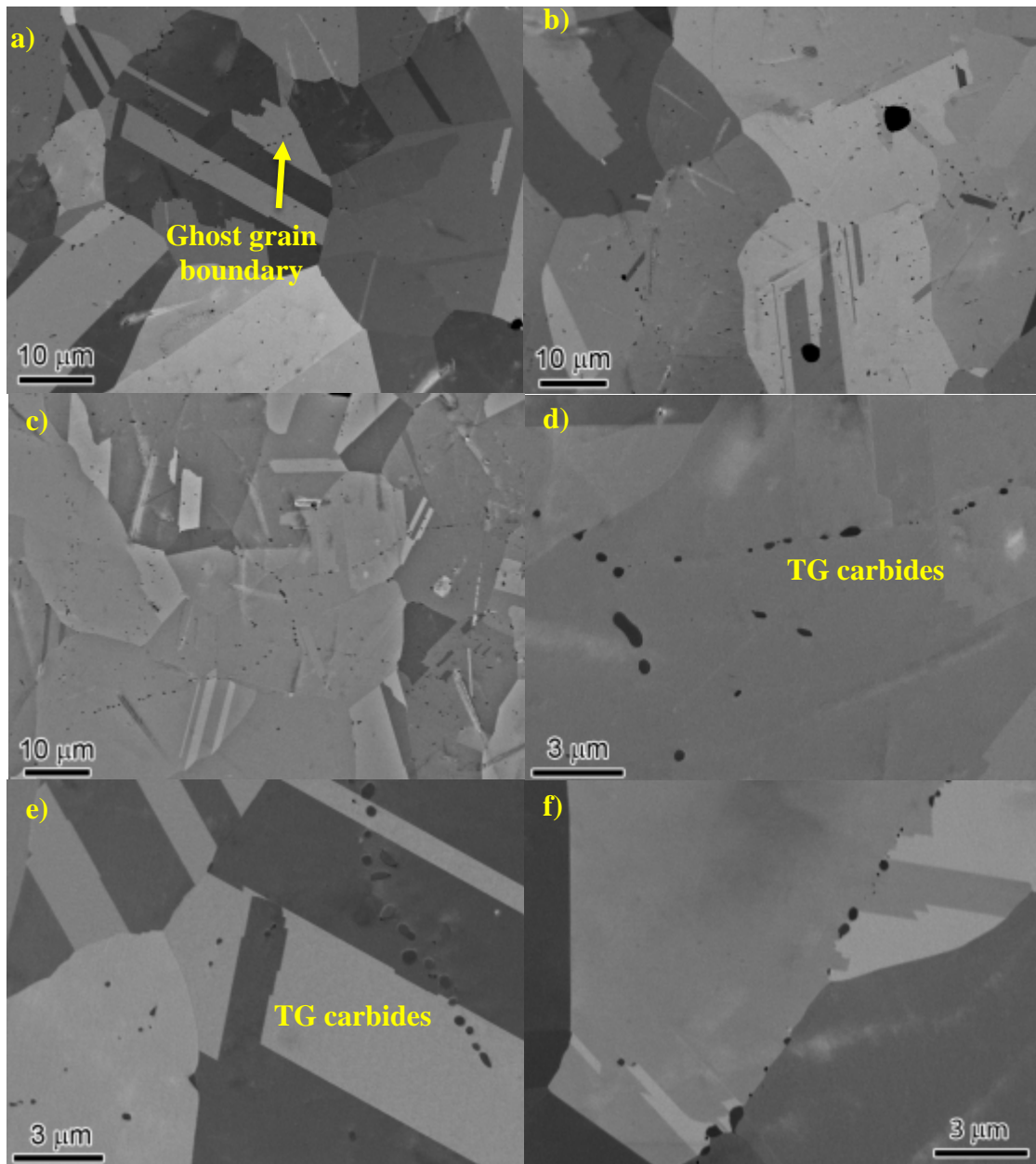


Figure 4. SEM-BSE images illustrating the general microstructures in the mill-annealed alloy 600 CRDM heat M7929 material.

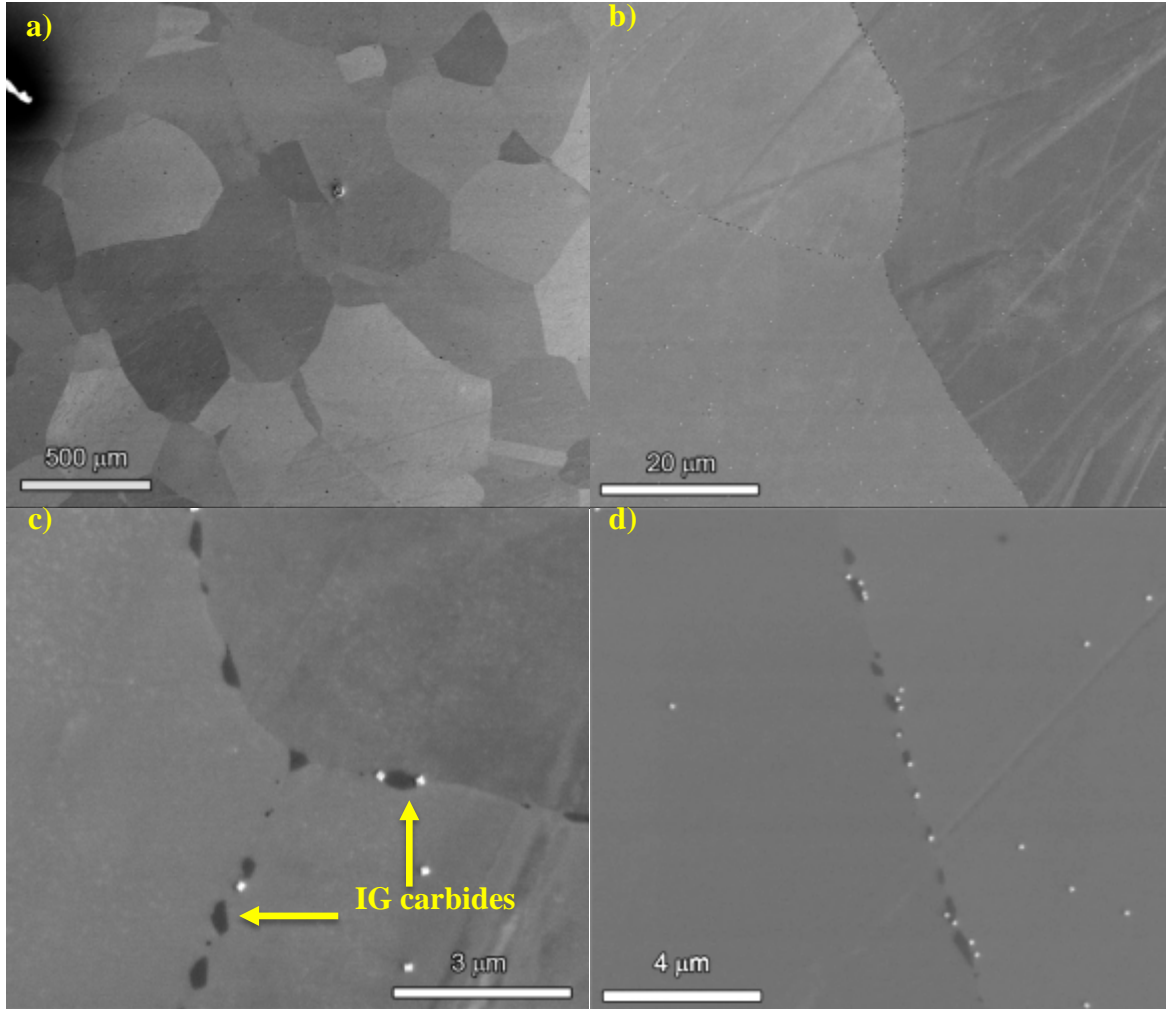


Figure 5. SEM-BSE images illustrating the general microstructures in the mill-annealed alloy 600 CRDM heat M3935 material. Small white particles in (c) and (d) are drying artifacts from the sample preparation process.

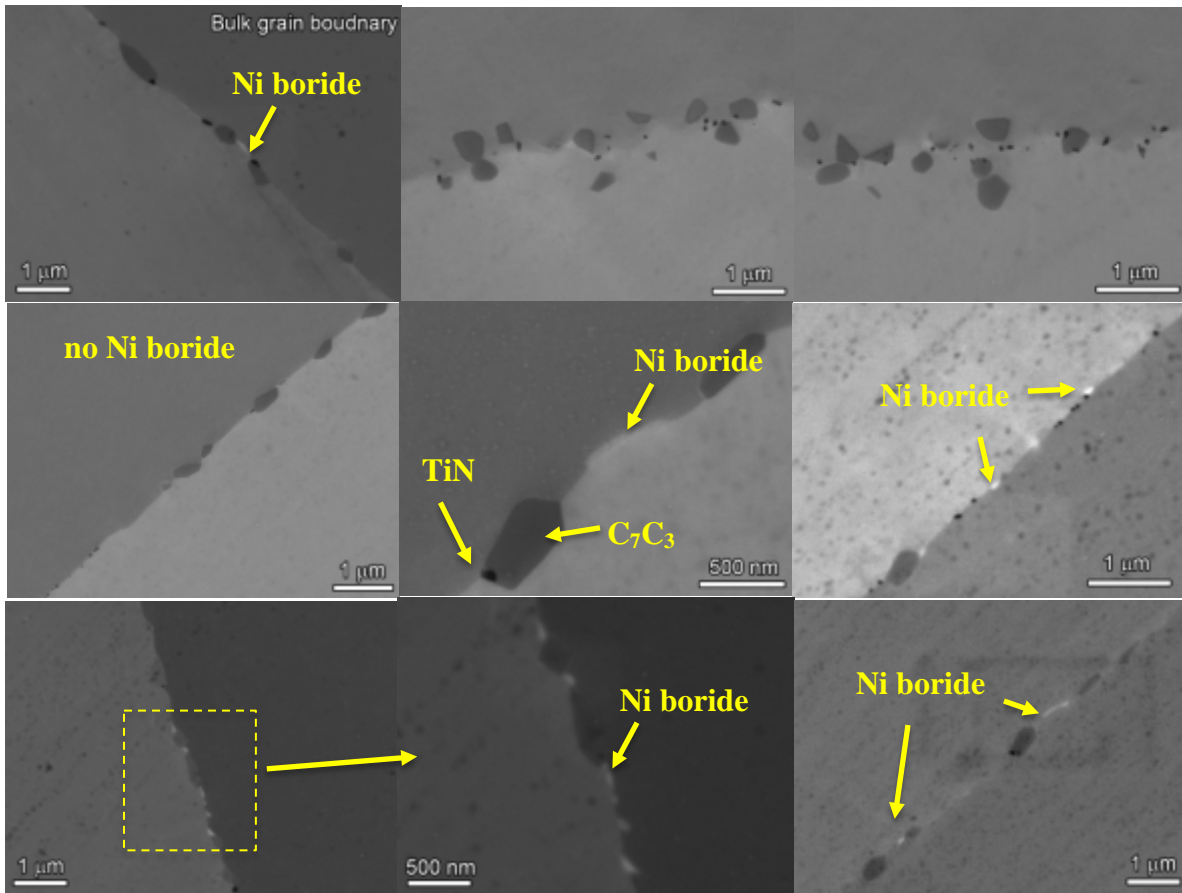


Figure 6. SEM-BSE images illustrating the general microstructures in the mill-annealed alloy 600 CRDM heat M3935 material at higher magnification illustrating the distribution of Cr₇C₃, TiN and Ni borides on the grain boundaries.

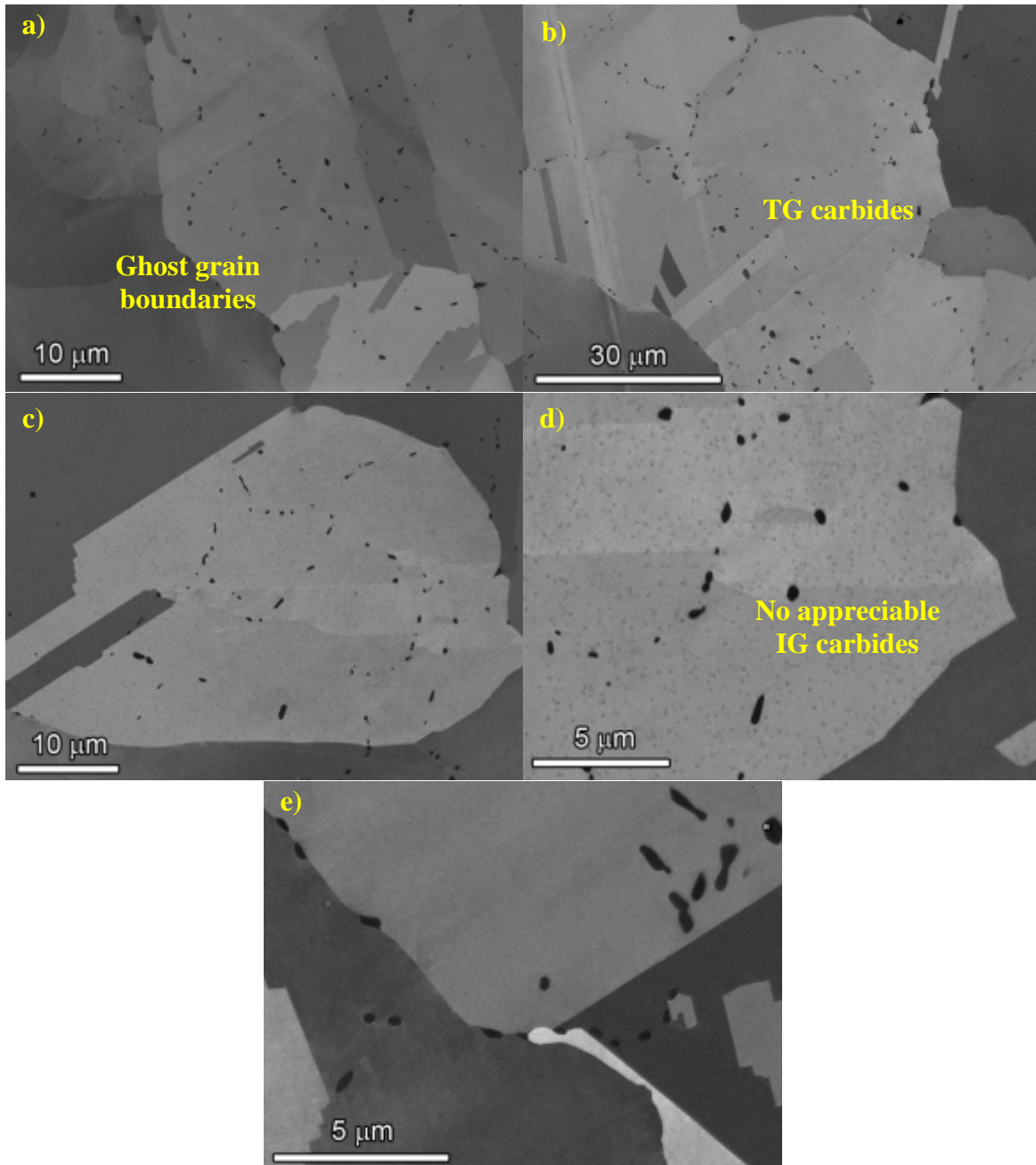


Figure 7. SEM-BSE images illustrating the general microstructures in the North Anna alloy 600 CRDM nozzle #31 material (NA2-N31).

Table 2. Microstructural characterization of alloy 600 materials.

Component	Heat or ID #	Grain Size (μm)	Strain Contrast	Primary Carbide Location	Carbide Density
Replacement Head Nozzle #4	Davis Besse M7929	~15	Low	TG on ghost grain boundaries	High
Original Head Nozzle #1	Davis Besse M3935	~300	Low	IG	500-700 nm spacing
CRDM Nozzle #31	North Anna 2 NA2-N31	~60	Low	TG on ghost grain boundaries	High

Additional characterizations were performed on the two Davis Besse heats using electron backscatter diffraction (EBSD) and hardness measurements. Overall general microstructure for heat M7929 as represented by EBSD is illustrated in Figures 8 and 9 revealing a small grain size (~15 μm diameter) and a moderate-to-high density of twins. Two different areas are shown from regions ~1.5 mm ahead of the final crack front of the SCC test specimen CT063 (DB-1). Area #1 lies right on the geometric crack path while area #2 is off to the side and overlaps slightly with area #1 as indicated by the reference points in the two figures. Misorientation density maps of these same two areas indicate small, discontinuous pockets of high strain.

A Vickers hardness map of a representative region from the side-surface cross-section sample is presented in Figure 10. Once again, this region is aligned ahead of the crack growth path for specimen CT063 and is near the EBSD examination locations. A region of locally higher hardness of ~210 kg/mm^2 is present in the map, however the average measured hardness was 186.5 kg/mm^2 with a standard deviation of 9.6 kg/mm^2 .

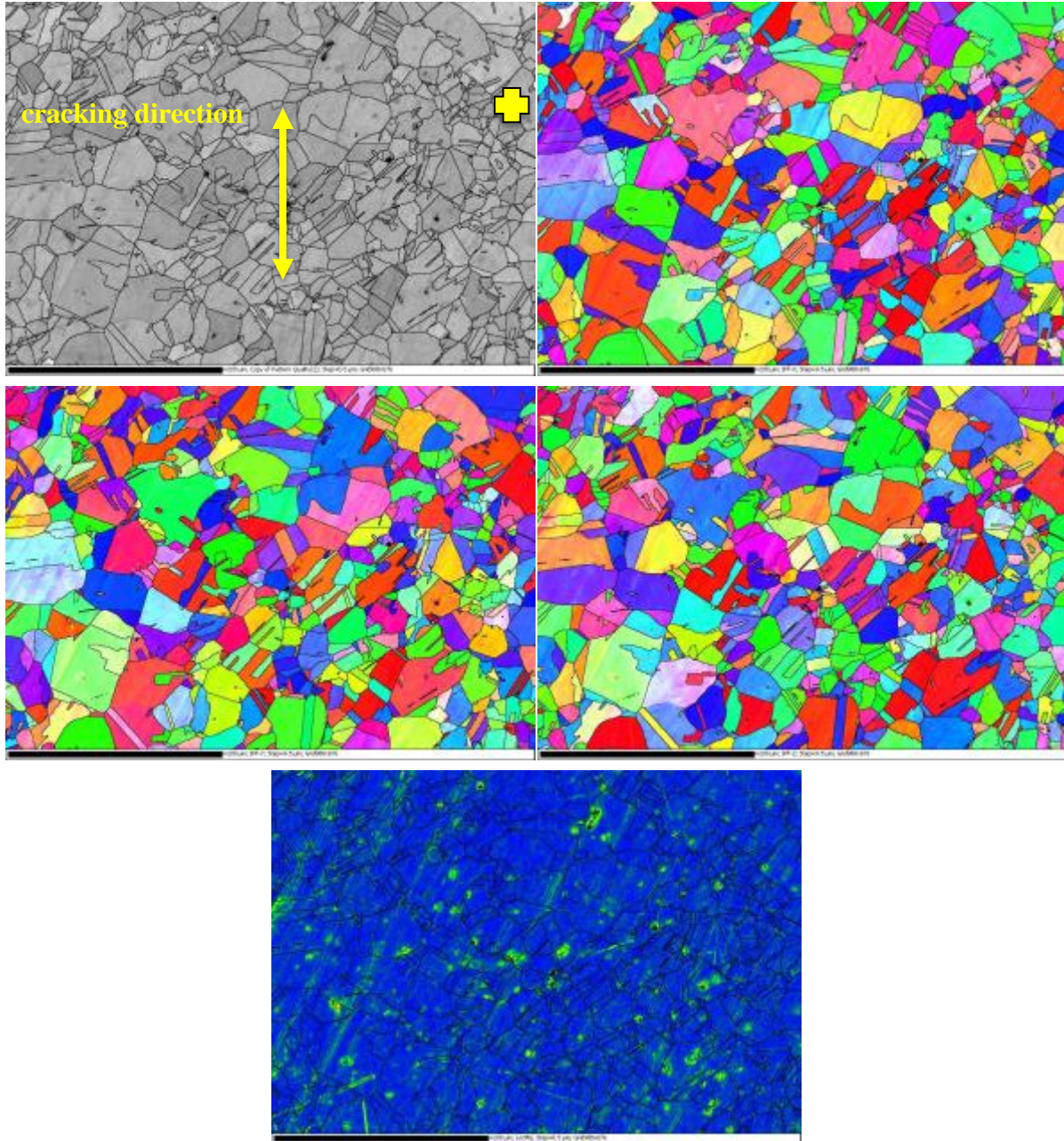


Figure 8. EBSD pattern quality map is shown in upper left image, inverse pole figure maps in upper right (X orientation), middle left (Y orientation) and middle right (Z orientation) images along with misorientation density map in bottom center for area #1 located ~1.5 mm head of the crack tip in the Davis Besse heat M7929, CT063 (DB-1) specimen crack growth plane. Yellow symbol in the pattern quality map is a reference overlap point for area #2 in Figure 9.

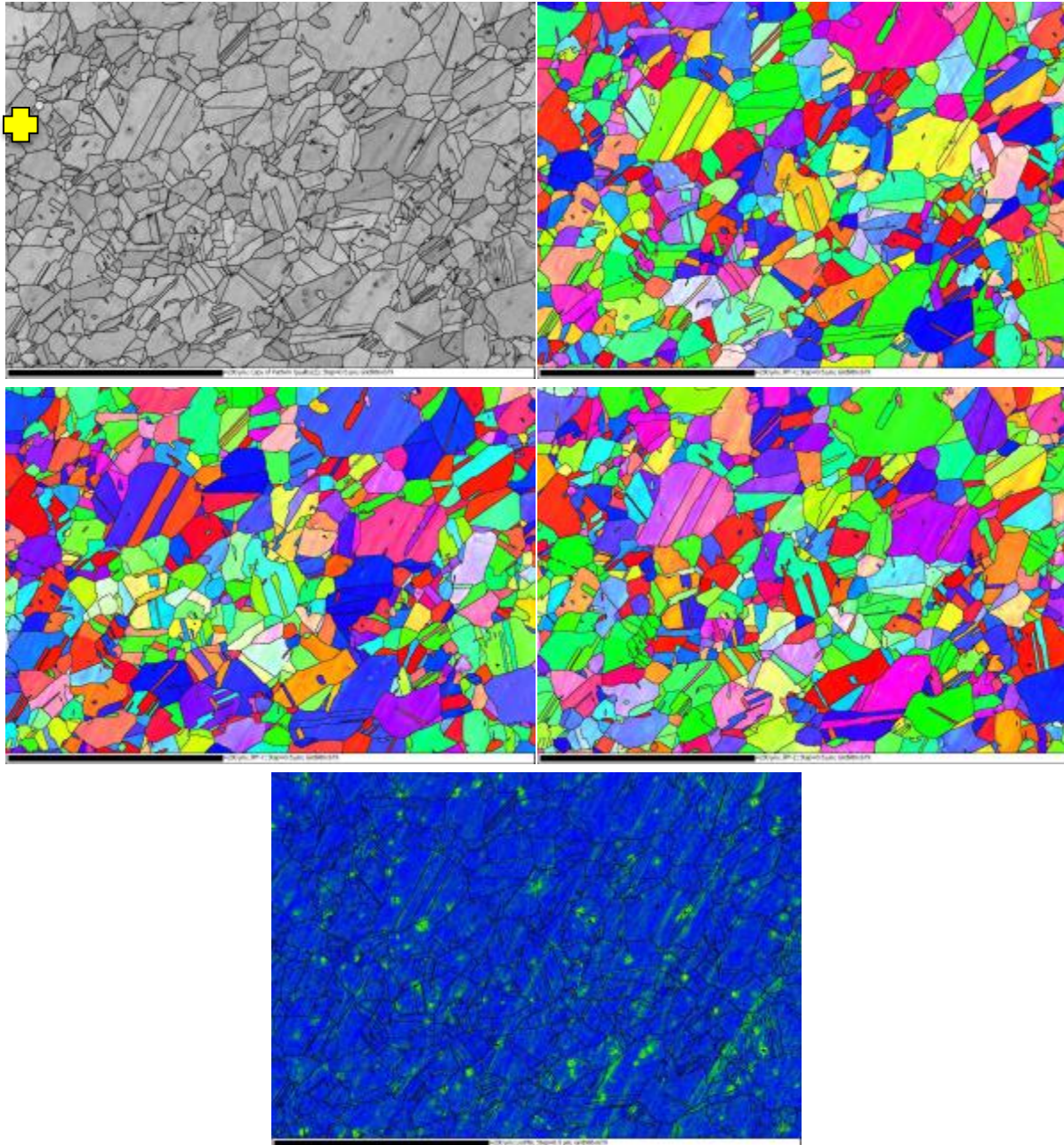


Figure 9. EBSD pattern quality map is shown in upper left image, inverse pole figure maps in upper right (X orientation), middle left (Y orientation) and middle right (Z orientation) images along with misorientation density map in bottom center for area #2 located off the crack plane adjacent to area #1 shown in Figure 8 for Davis Besse heat M7929. Yellow symbols in pattern quality maps show reference overlap point between area #1 and area #2.

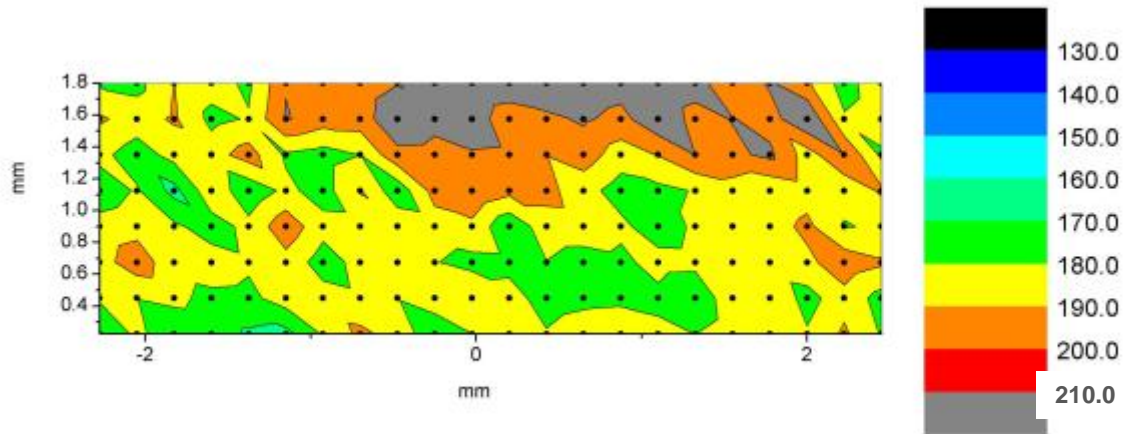


Figure 10. Vickers hardness map for Davis Besse heat M7929, CT063 specimen crack growth plane. The average measured hardness was 186.5 kg/mm^2 with a standard deviation of 9.6 kg/mm^2 .

The overall general microstructure for heat M3935 is represented by EBSD in Figure 11 revealing the extremely large grain size and a very low density of twins. This area is from a region ~ 1 to 1.5 mm ahead of the final crack front along the geometric crack path in the SCC test specimen CT090 (DB-H1N1 #1). Consistent with the lack of deformation twins, the misorientation density map of this area reveals low strains.

A Vickers hardness map of a representative region from the side-surface cross-section sample is presented in Figure 12. Once again, this region is aligned with the geometric crack path for specimen CT090 and is near the EBSD examination location. With the exception of a single indentation that produced a hardness of $\sim 180 \text{ kg/mm}^2$, this region exhibited a consistent hardness of 160.2 kg/mm^2 with a standard deviation of 6.5 kg/mm^2 .

Distinctive differences can be seen comparing the microstructures and hardness results for the two alloy 600 CRDM materials from Davis Besse in Table 2. The replacement head nozzle heat M7929 has a small grain size for a thick-wall CRDM tube, a moderate density of twins, few IG carbides with virtually all carbides on prior (ghost) grain boundaries, evidence of residual strain (misorientation map) and a slightly higher measured hardness. The original head nozzle heat M3935 has a very large grain size, no twins, primarily IG carbides, no evidence of residual strain and lower measured hardness. Surprisingly, the mill specs for these materials show that the M3935 tubing is supposed to have a $\sim 13\%$ higher yield strength than the M7929 tubing. This is not consistent with the current measurements on materials removed from PWR service.

No EBSD or hardness measurements were made on the North Anna 2 nozzle 31 material but will be obtained in the future if SCC growth tests are performed.

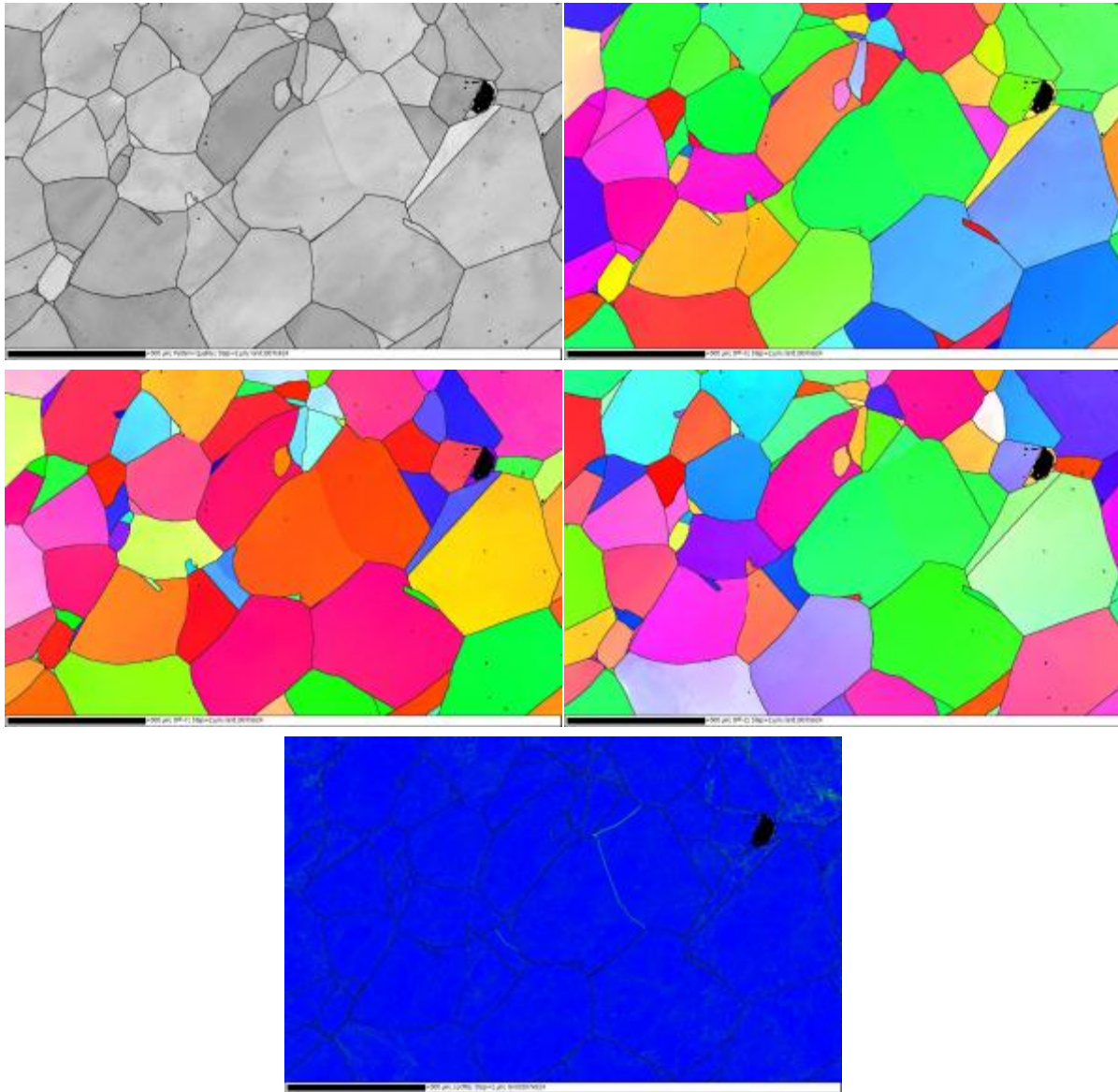


Figure 11. EBSD pattern quality map is shown in upper left image, inverse pole figure maps in upper right (X orientation), middle left (Y orientation) and middle right (Z orientation) images along with misorientation density map in bottom center for Davis Besse heat M3935, CT090 specimen crack growth plane.

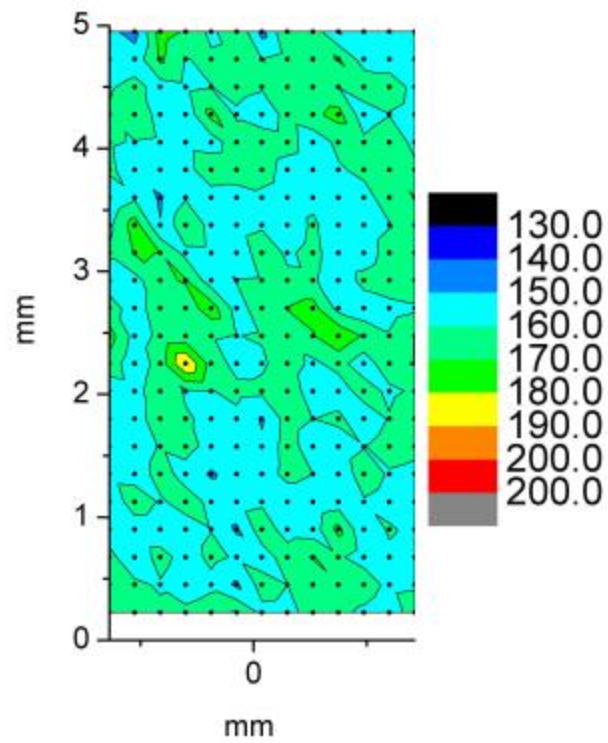


Figure 12. Vickers hardness map for Davis Besse heat M3935, CT090 specimen crack growth plane. The average measured hardness was 160.2 kg/mm^2 with a standard deviation of 6.5 kg/mm^2 .

Transmission Electron Microscopy (TEM) Examinations on Alloy 600 Heats

Limited TEM examinations were performed on high-angle grain boundaries from each of the two Davis Besse heats to investigate grain boundary precipitate distributions and local compositions. Figure 13 shows a TEM brightfield images (left) and energy dispersive x-ray spectroscopy (EDS) line scans (right) from two grain boundaries for the heat M7929 material. Consistent with the SEM results, no grain boundary carbides were identified and there was no evidence for Cr depletion or impurity segregation.

An SEM-BSE image of a FIB machined TEM plate sample from heat M3935 is shown in Figure 14. A high density of Cr carbides and sporadic TiN are observed along the grain boundary. Unlike the majority of SEM BSE images of this material in Figure 6, there are no apparent bright intergranular phases (Ni borides). It is possible that this section of grain boundary does not contain any. Using diffraction and darkfield imaging (Figures 15 and 16), the Cr rich carbides were determined to be primarily Cr_7C_3 . STEM brightfield and EDS elemental maps of the Cr_7C_3 and TiN precipitates are shown in Figures 17 and 18. Lastly, significant Cr depletion was identified to levels below 10 wt% in EDS line scans of grain boundary regions that did not contain carbides (Figure 19). More detailed analyses of grain boundary composition were made using atom probe tomography (APT) and is described in the following section. Both the TEM and APT characterizations were conducted under funding from a Department of Energy, Office of Basic Energy Sciences project at PNNL.

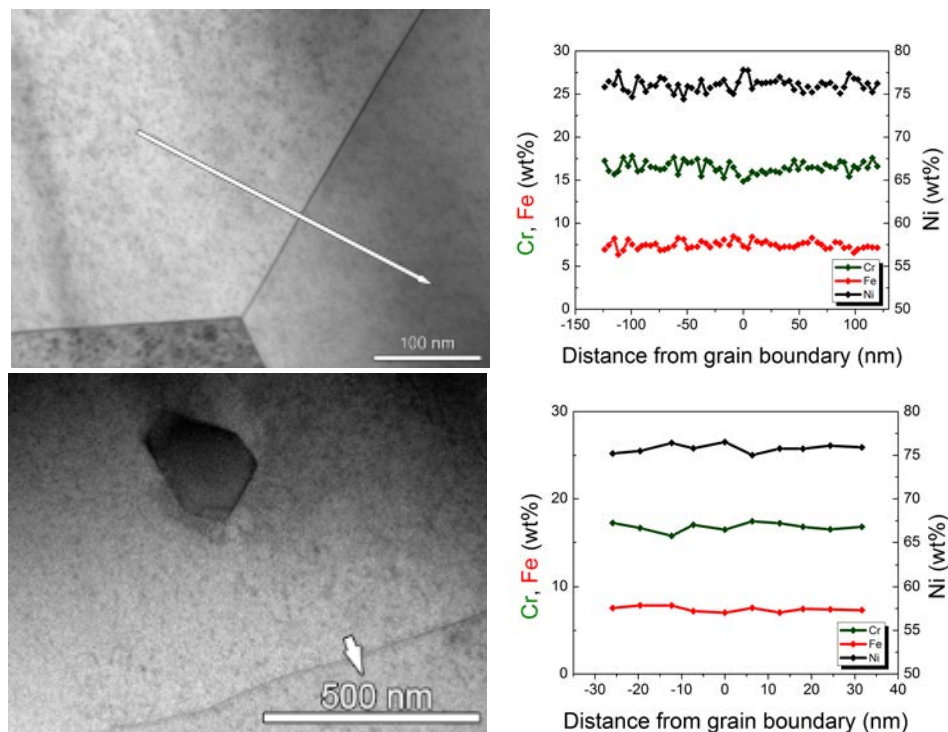


Figure 13. STEM EDS line scans across two grain boundaries in alloy 600 M7929 showing little to no Cr depletion.

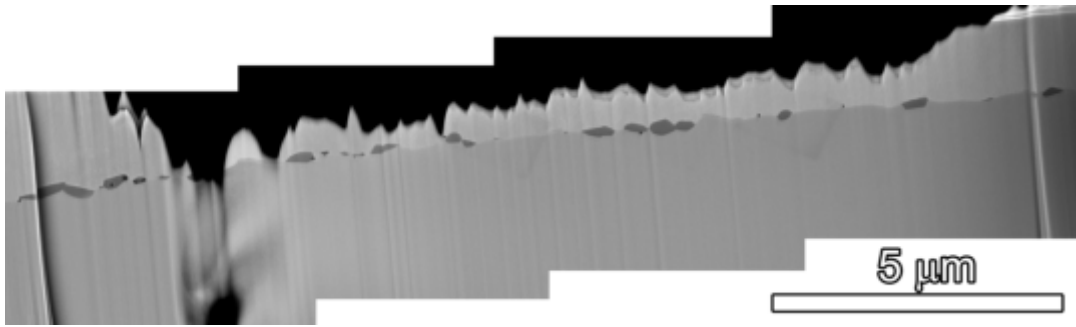


Figure 14. SEM-BSE montage of FIB machined TEM plate sample containing a grain boundary from alloy 600 M3935. In this region, there does not appear to be any Ni boride particles.

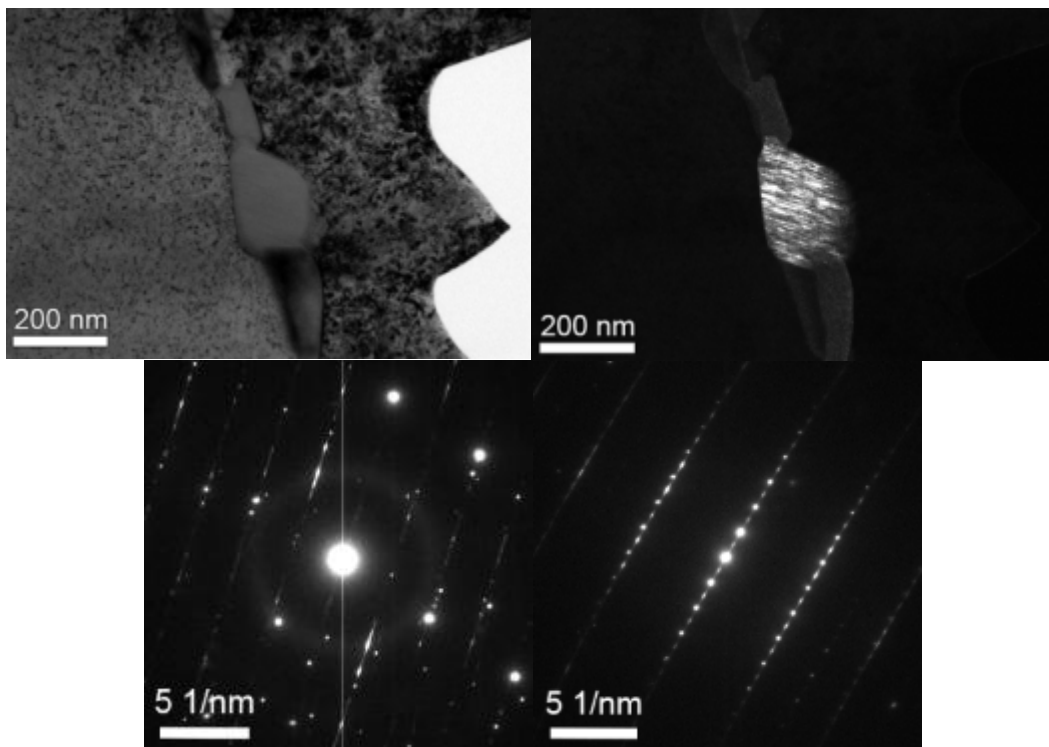


Figure 15. TEM BF/DF pair and selected area diffraction patterns of an IG Cr_7C_3 carbide in the alloy 600 M3935 material.

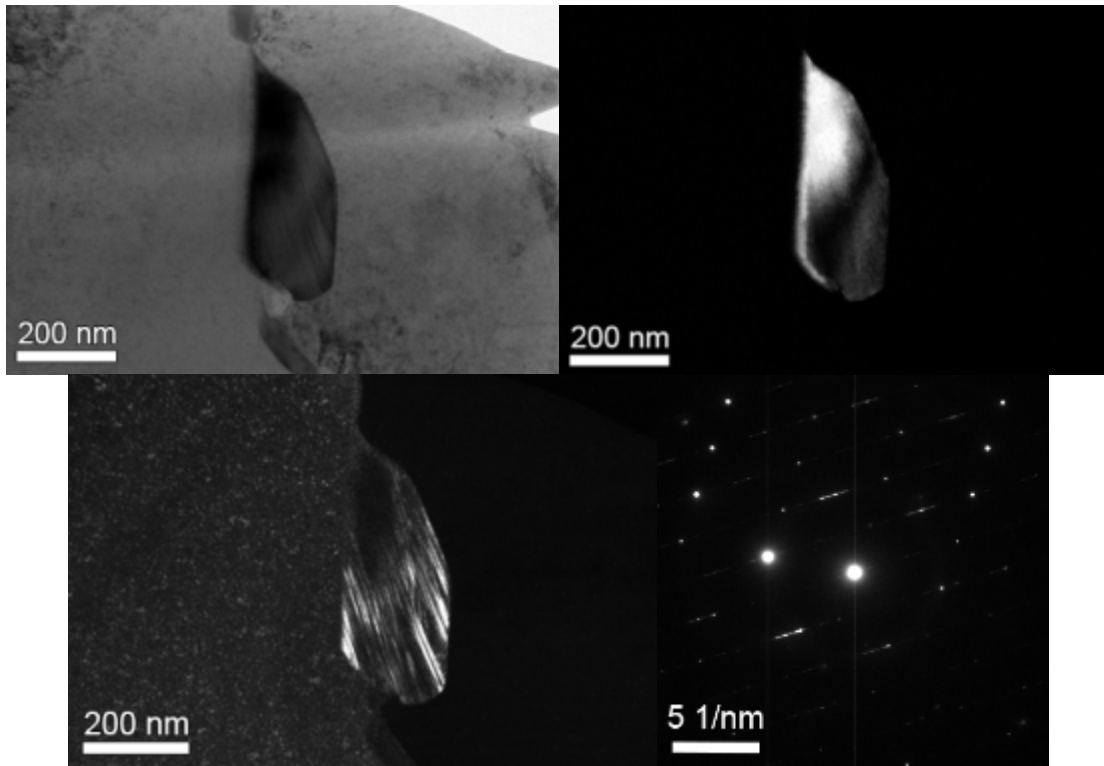


Figure 16. TEM BF/DF pair and selected area diffraction of an IG Cr_7C_3 carbide (two different reflections are used to illuminate the carbide) in the alloy 600 M3935 material.

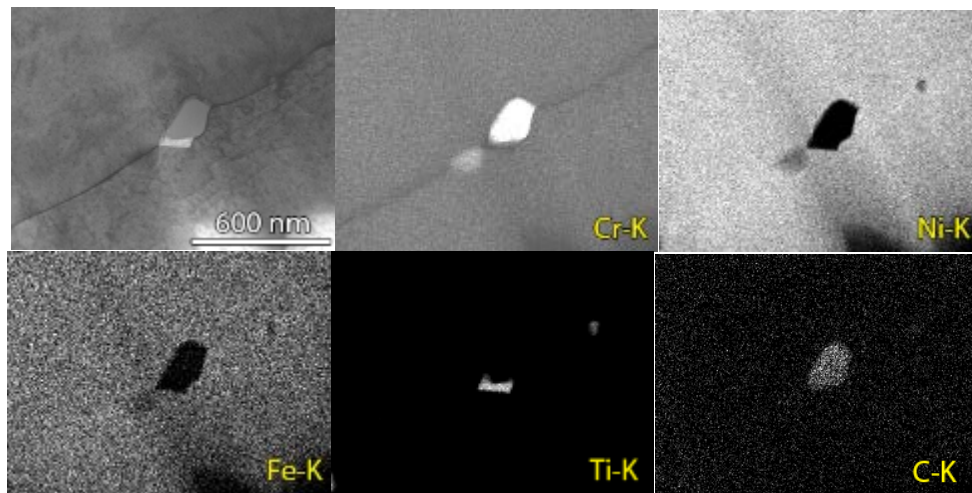


Figure 17. STEM/EDS elemental maps of a grain boundary in alloy 600 M3935. A ~ 100 nm, IG M_7C_3 carbide is observed on the grain boundary. Smaller (25-50 nm) Ti rich particles are also observed. With the grain boundary nearly on edge (as seen in the BF image), local Cr depletion is evident in the Cr-K map.

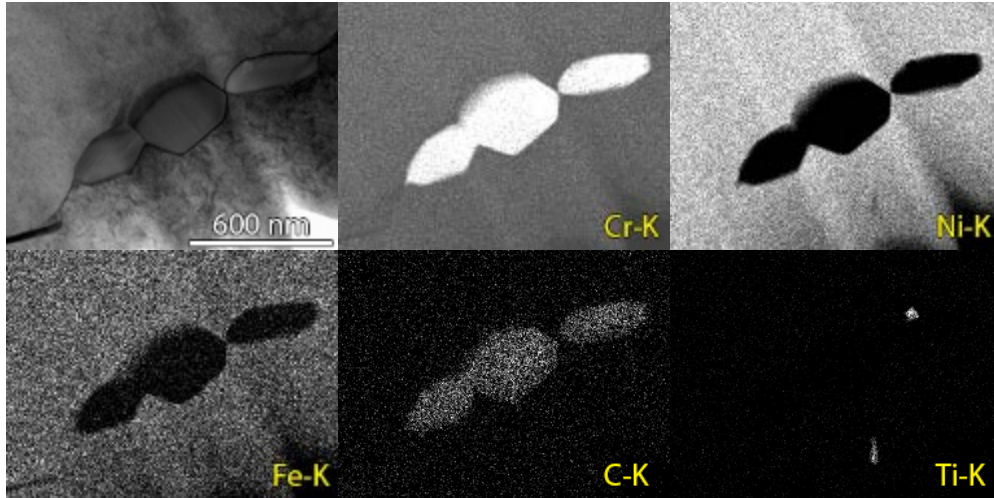


Figure 18. STEM/EDS elemental maps from a second region of the M3935 grain boundary.

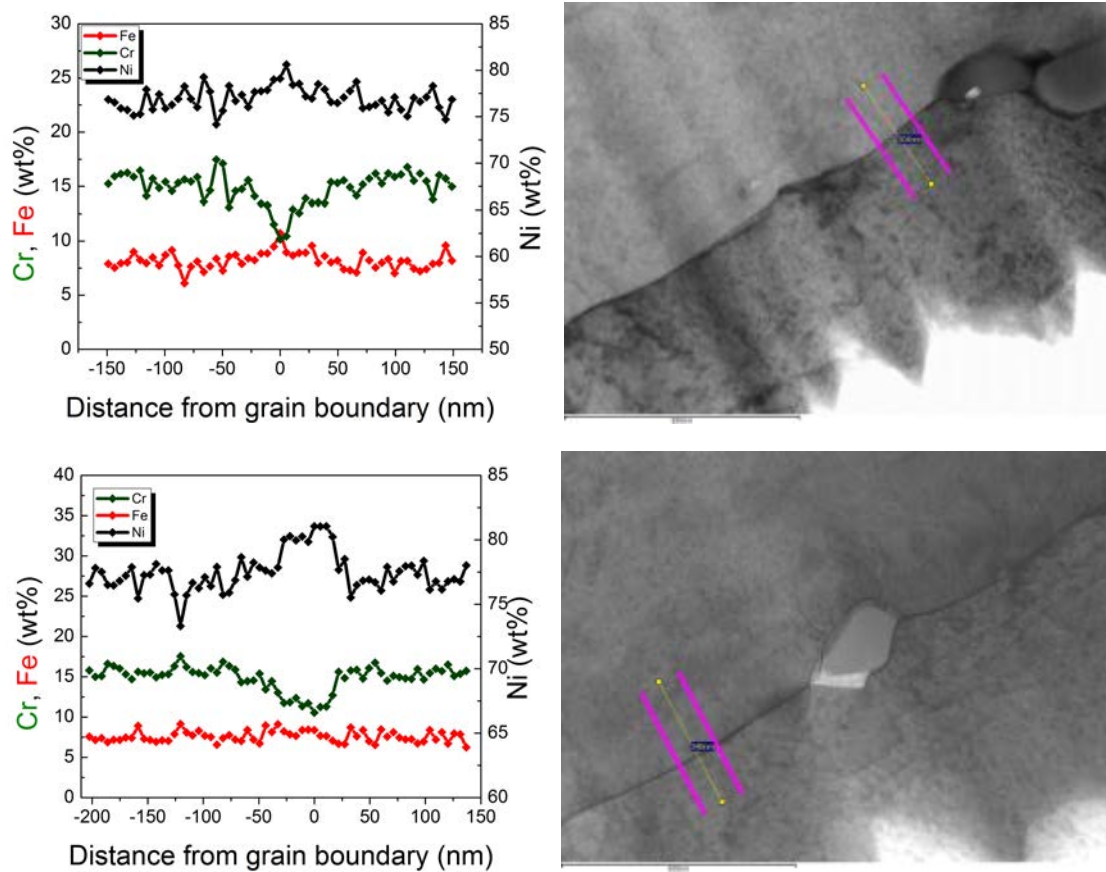


Figure 19. EDS line scans taken across two regions along the same grain boundary in alloy 600 M3935. The chromium depletion is observed to ~10-11 wt% in either lines can, with the top lines can showing a slightly sharper profile. From the top STEM BF image, it is readily apparent that the grain boundaries are not completely straight and are observed to be inclined even at distances of 500 nm apart.

Atom Probe Tomography (APT) Characterizations on Alloy 600 Heats

Much attention has been given to the role of microstructure on the SCC susceptibility of alloy 600 materials in PWR primary water. These studies, typically leveraging optical, SEM and TEM microanalyses, have identified some microstructural features as being advantageous or detrimental to SCC resistance. The most frequent observation seems to be the beneficial effect of a high density of IG Cr carbides. Conversely, a low density of IG Cr carbides and a high density of TG carbides have been suggested to be detrimental to SCC resistance. Despite these generalizations, some heats of alloy 600 exhibit unexpectedly high SCC susceptibility despite typical or supposedly SCC-resistant microstructures. One possible explanation for this variability in SCC response may be unexpected and previously unobserved segregation of difficult-to-detect species to the grain boundary.

APT is one technique that is capable of analyzing grain boundary segregation of nearly all species independent of atomic number. This is particularly advantageous to describing the segregation of light elements (e.g. B, P and C) in small concentrations that are difficult to describe by ATEM. Early applications of APT were plagued by small datasets and thus poor counting statistics that were inherent to the technique at that time. Since these early studies, relatively little attention has been given to alloy 600 grain boundary segregation using modern APT instrumentation that can provide dramatically improved counting statistics and thus quantitative accuracy. To put the difference in perspective, the matrix compositions reported in one of these previous studies were based on datasets containing between 3,000 and 18,000 detected ions. With modern instrumentation, a “small” dataset consists of >2,000,000 ions and more typically contains on the order of 10,000,000 ions. The improved counting statistics negate the effect of counting error on the resulting quantitative measurements. Such an improvement in data size results in the error of compositional measurements being dominated not by counting statistics but instead being a measure of variability from specimen to specimen or grain boundary to grain boundary. Therefore, it is very beneficial that grain boundary composition be revisited as a potential contributor to SCC susceptibility utilizing modern APT instrumentation.

APT analyses have now been performed on general, high-angle grain boundaries for seven alloy 600 materials including 3 CRDM nozzle, 3 steam generator tube and a steam generator divider plate heats. Results for the Davis Besse and North Anna 2 CRDM nozzle materials (provided by this project) are shown here.

APT analyses were performed on the two alloy 600 CRDM nozzle materials from Davis Besse heats M7929 (from the replacement head) and M3935 (from the original head) that exhibited high susceptibility to IGSCC in service. One successful APT analysis was obtained from a random high-angle grain boundary in M7929 and two runs were successfully performed on grain boundaries from M3935. As will be shown below, both of these heats exhibited particularly strong B segregation.

Representative atom maps from M7929 are depicted in Figure 20. Strong grain boundary segregation is apparent for B, Mg and P. The extent of segregation is quantified in Figure 21 using a proximity histogram across the boundary. This profile confirms strong segregation for B (2.6 at%), Mg (0.5 at%) and P (0.15 at%). By comparison, the Cr depletion observed (minimum 11.5 at%) is minor for a material that exhibited moderate grain boundary coverage of IG Cr

carbides. No detectable segregation was observed for Si, which is somewhat surprising as most of the other alloy 600 materials that have been examined at PNNL have exhibited at least some Si grain boundary enrichment.

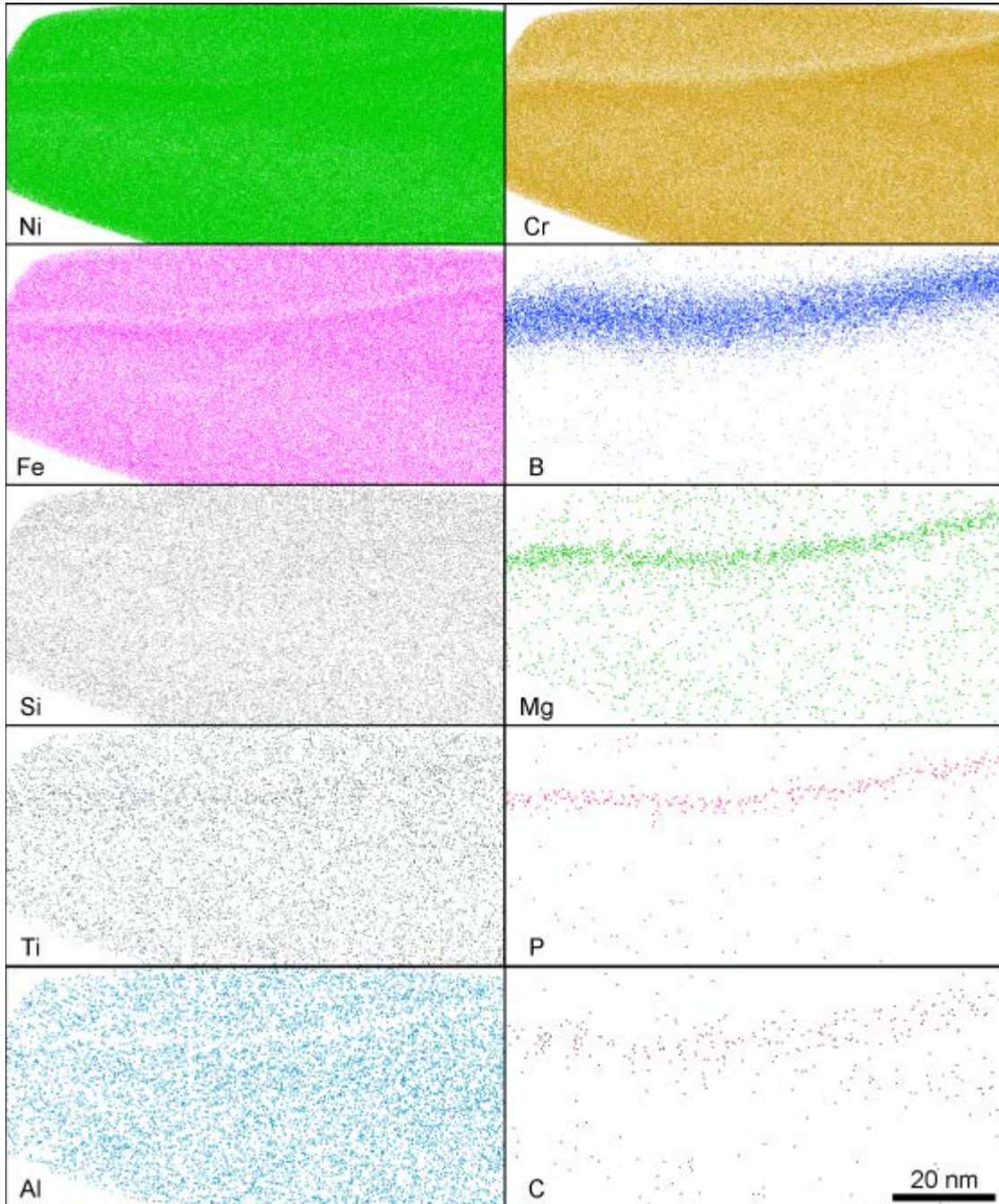


Figure 20. Atom maps (20 nm image depth) from Davis Besse CRDM heat M7929. Particularly strong segregation is apparent for B, Mg and P.

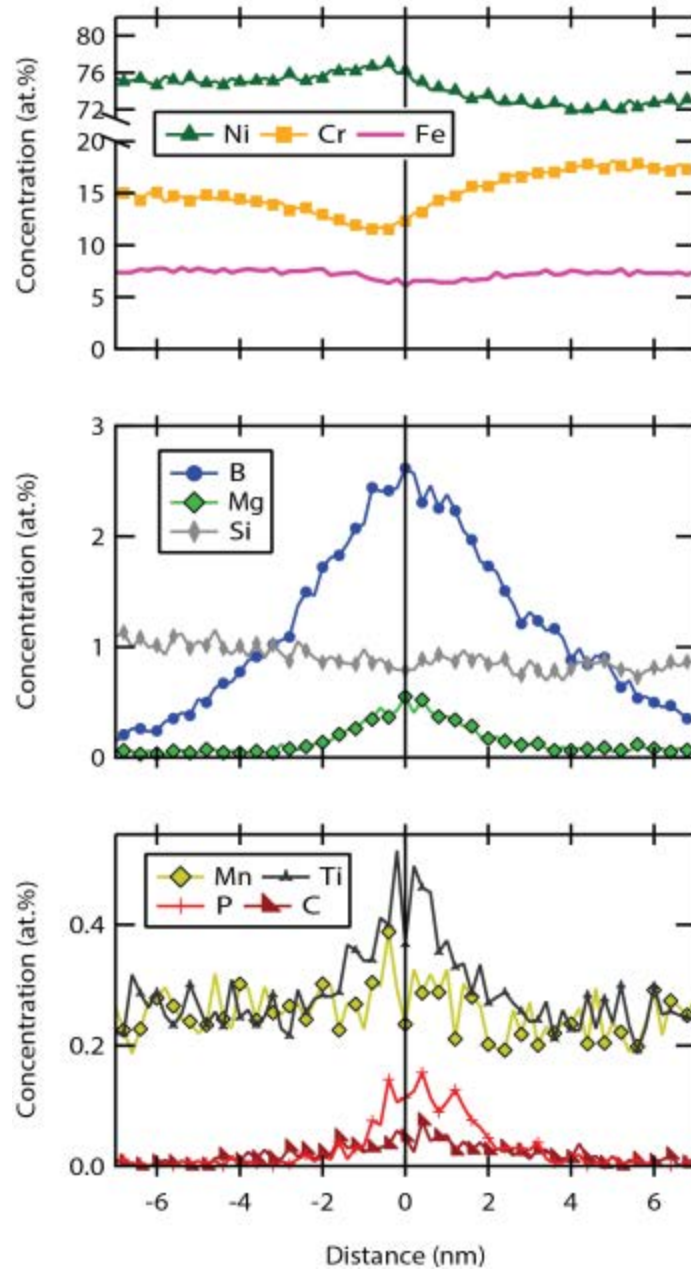


Figure 21. Proximity histogram taken across a high-angle grain boundary in Davis Besse CRDM heat M7929. Very strong interfacial segregation is apparent for B, Mg, Ti and P. Minor Cr depletion and Ni enrichment are also apparent.

Two APT specimens from heat M3935 were collected intersecting IG precipitates. The first specimen was found to contain a Ti carbo-nitride covering the grain boundary across the entire width of the APT needle. The corresponding APT reconstruction is presented in Figure 22. The carbo-nitride precipitate is strongly enriched in Ti, C and N and strongly depleted of Ni, Fe, Al and Mn. Interfacial segregation is apparent for B and P. Note that peak overlap between $^{28}\text{Si}^{2+}$ and $^{14}\text{N}^{1+}$ prevents the analysis of any potential Si segregation in this specimen. A proximity histogram was produced at the carbo-nitride/metal interface to quantify both the precipitate composition and the interfacial segregation (Figure 23). The precipitate consists of ~50 at% Ti, 33 at% N, 6 at% C and 6 at% Cr. Interfacial segregation is very significant. Pronounced enrichment is apparent for B (to ~2.5 at%) and P (to 0.08 at%). Chromium exhibits a more complicated behavior in which some enrichment is apparent at the metal/precipitate interface, while Cr depletion also exists just outside this enriched interface, down to ~11 at%. Interfacial segregation to ~8 at% is also indicated for C.

A second APT dataset on M3935 was collected on a needle containing an IG Cr carbide precipitate. Representative atom maps from this dataset are presented in Figure 24. A Cr carbide precipitate is apparent at the specimen apex and is surrounded by very strong B segregation and Cr depletion. A small region of metal/metal grain boundary is also apparent, extending past the bottom-right corner of the carbide particle to the edge of the APT needle reconstruction. Very strong, pockets of Cr and Fe depletion along the carbide periphery (arrowed) correspond to localized enrichment of B, which could suggest that the carbide/metal interface is decorated by nanoscopic Ni boride precipitates.

Concentration profiles were produced across the metal/metal grain boundary adjacent to the IG carbide and also from the carbide/metal interface in Figure 25. Each profile quantifies extraordinarily high levels of interfacial B segregation up to 5 at% B and 11 at% B at the metal/metal and carbide/metal interfaces, respectively. These represent the highest levels of B segregation among alloy 600 examined by PNNL. Similar to the other CRDM heat (M7929), the grain boundary does not exhibit any detectable segregation of Si. Slight segregation is apparent for C, P, Mn and Ti at the grain boundary. IG Cr depletion, expected to be severe in such close proximity to an IG Cr carbide, was only moderate, with a minimum value of ~8 at% Cr. In general, the carbide/metal interface was very similar to the metal/metal grain boundary. Cr was depleted to ~7 at%, while slight segregation was seen for P and Ti with no Si enrichment.

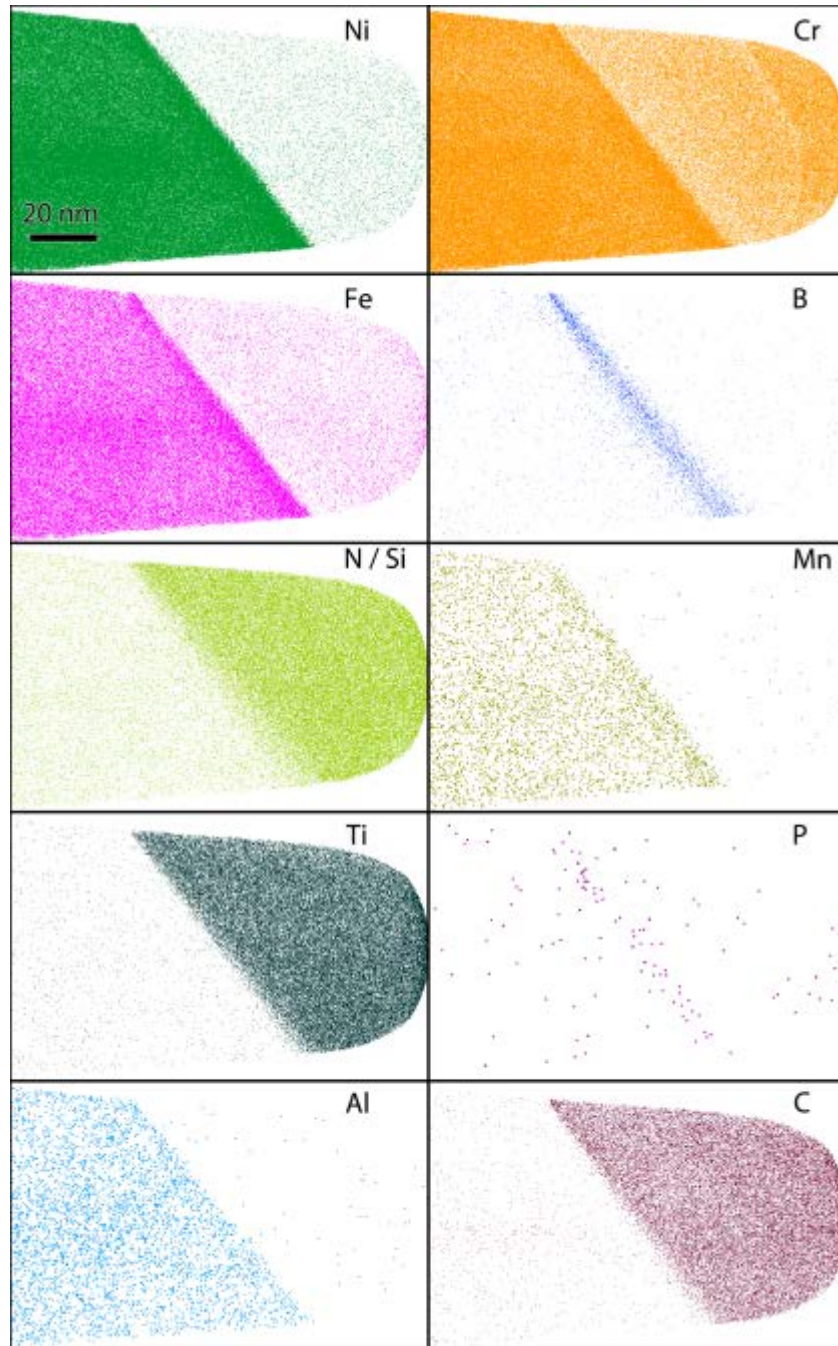


Figure 22. Atom map (10 nm image depth) of an IG Ti carbo-nitride in Davis Besse CRDM heat M3935. Strong interfacial segregation is apparent for B and weak segregation for P. Note that Si and N peaks are convoluted with one another and impossible to differentiate.

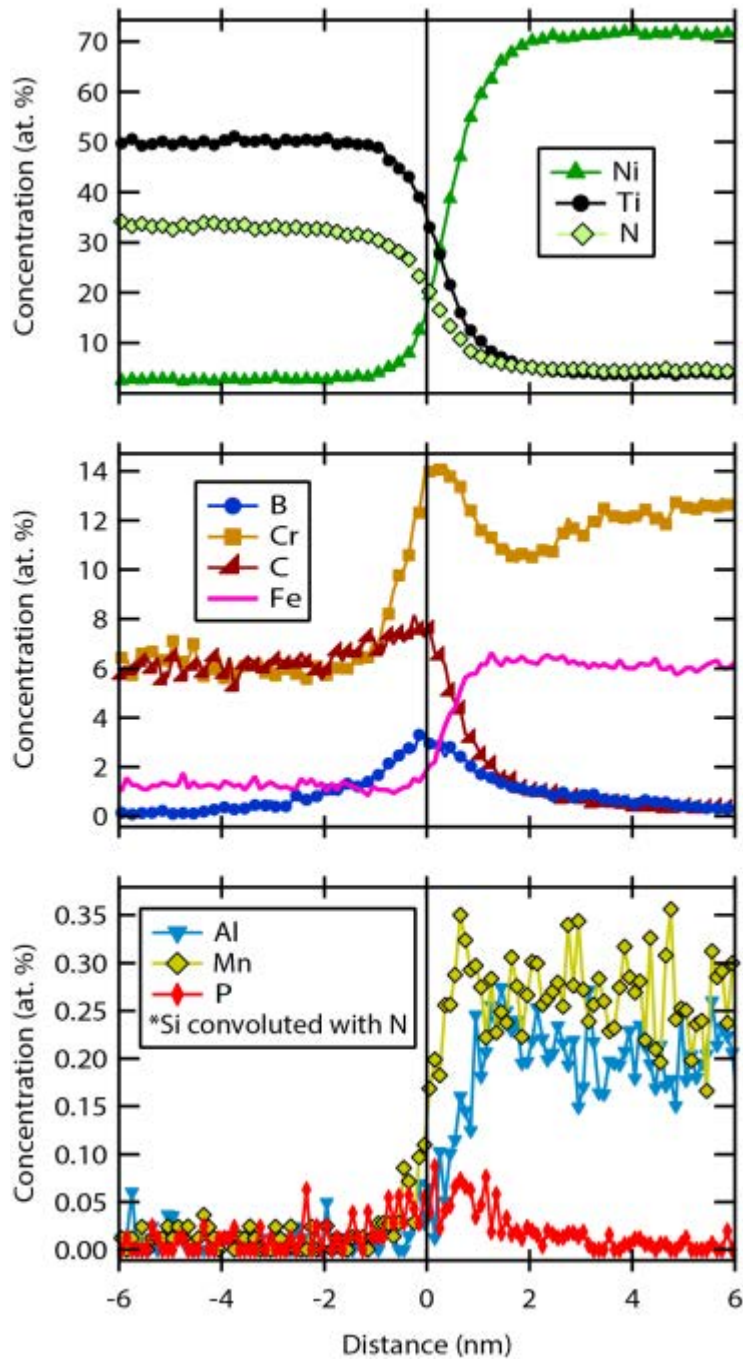


Figure 23. Proximity histogram across the Ti carbo-nitride/metal matrix interface in M3935. The precipitate contains a moderate concentration of Cr that is also strong segregated to the interface. B is strongly segregated (~3.3 at%) along with a small enrichment of P (~0.06 at%).

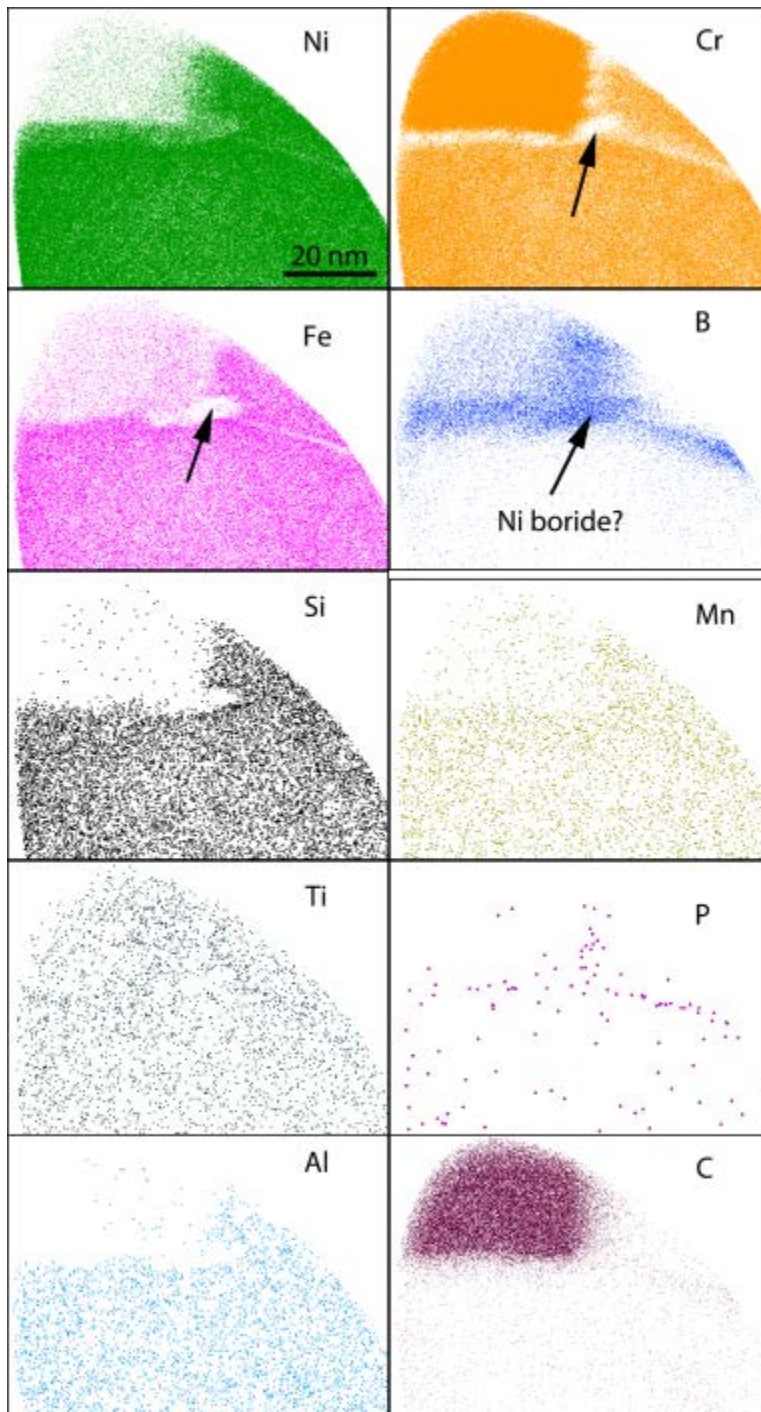


Figure 24. Atom maps from an IG Cr carbide and surrounding grain boundary in Davis Besse CRDM heat M3935. Very strong Cr depletion and B enrichment are apparent along the grain boundary and metal/carbide matrix. Particularly strong localized B enrichment and Cr depletion is suggestive of possible Ni boride precipitations (arrowed).

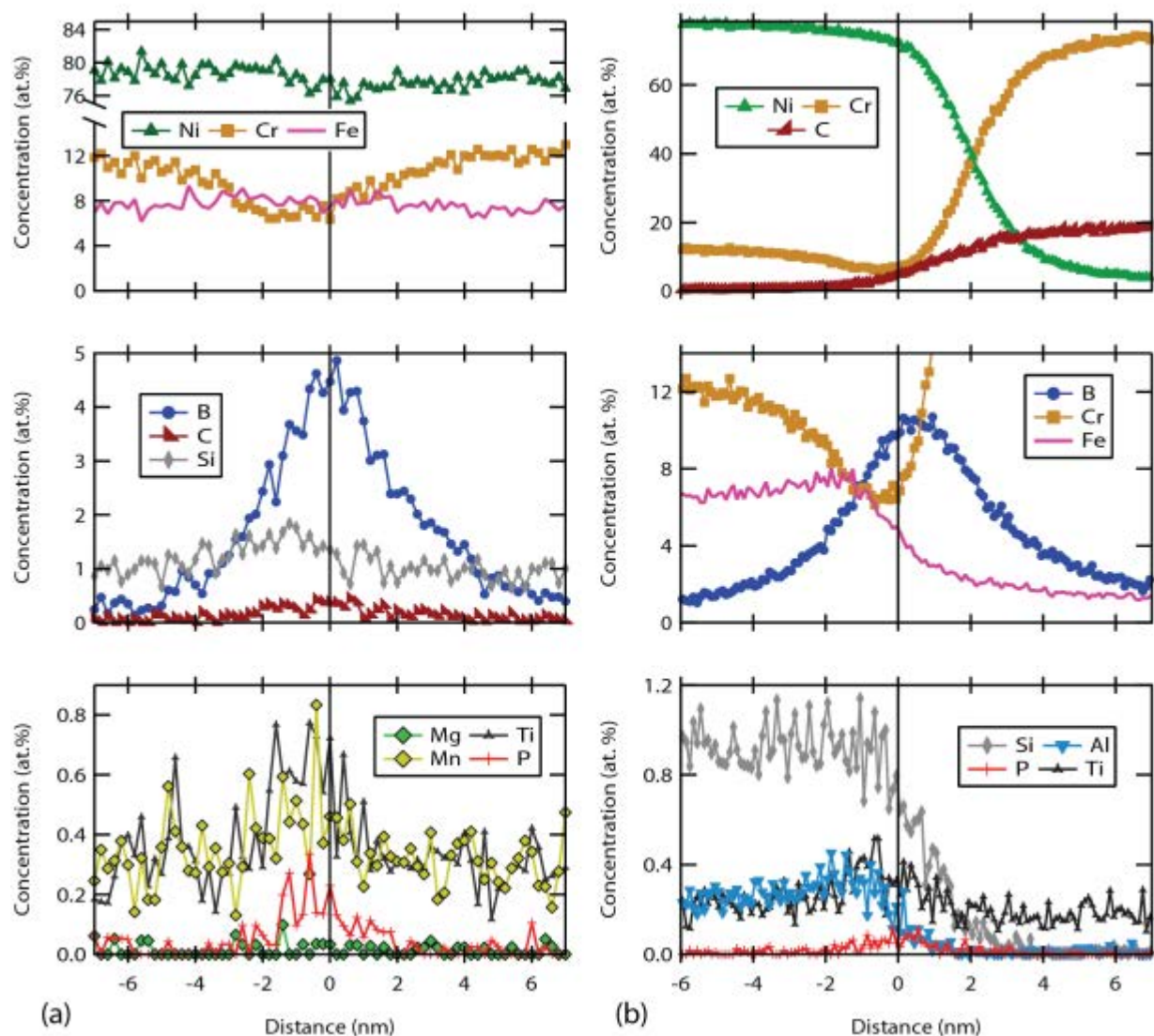


Figure 25. Concentration profiles across (a) the metal/metal grain boundary and (b) across the IG Cr carbide / metal interface in Davis Besse CRDM heat M3935. Both types of interfaces exhibit particularly strong B segregation (5 at% and 11 at%, respectively) and Cr depletion (<8 at% each). Relatively strong P segregation is apparent at each interface (~0.2 at%) and no significant Si segregation is observed.

As mentioned when discussing the atom maps of this dataset, the extraordinarily high levels of B and localized Cr depletion at the carbide/metal interface suggest the possibility of Ni boride precipitation at the carbide/metal interface. To better visualize this possibility, a full three-dimensional reconstruction (rather than a thin two-dimensional slice of data) is presented in Figure 26. The three-dimensional morphology of the carbide is defined using a 5 at% C isoconcentration surface (maroon). Localized regions of particularly high B concentrations are defined along the carbide/metal interface with 13 at% B isoconcentration surfaces (blue).

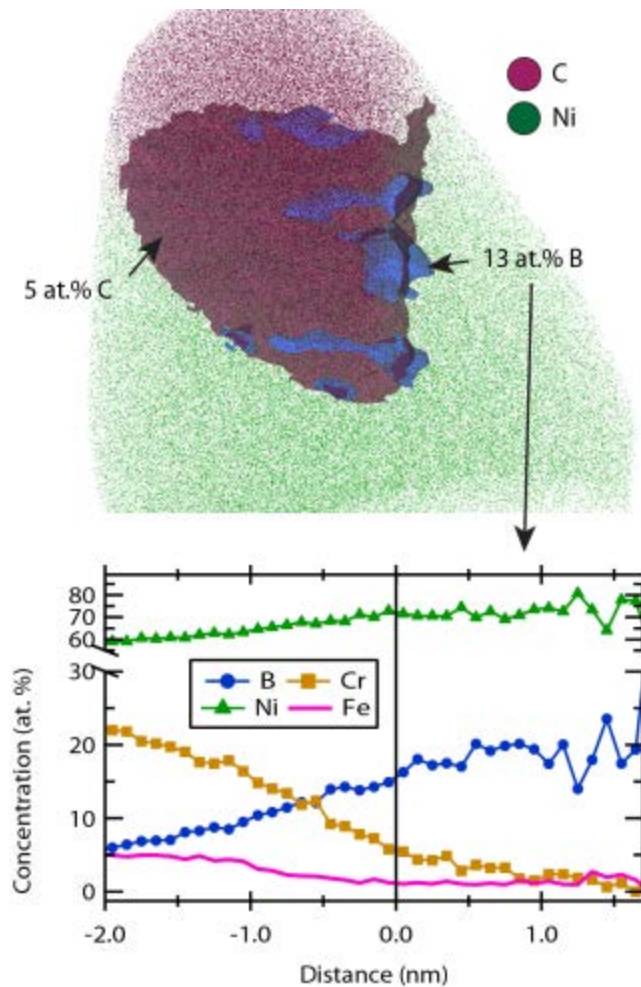


Figure 26. APT reconstruction of the IG carbide in the Davis Besse CRDM heat M3935. Isoconcentration surfaces at 5 at% C (maroon) and 13 at% B (blue) outline the Cr carbide and possible Ni boride, respectively. A proximity histogram (bottom) from around the 13 at% B isoconcentration surface confirms the coincident enrichment of Ni and B (up to 20 at%) that is suggestive of an interfacial Ni boride phase.

Numerous small islands of B enrichment decorate the interface especially near the lower-right corner where the carbide meets the metal/metal grain boundary. A proximity histogram is plotted below the three-dimensional reconstruction. The center of the B enrichment peaks at ~20 at% B and coincides with very strong Cr depletion to less than 2 at% Cr. Considering that APT typically underestimates B concentrations, it is plausible that these B-rich particles could be Ni_{23}B_6 . Careful examination of similar IG carbides by TEM was unable to reveal similar nanoscopic boride precipitates. It is unclear right now whether this is because of an absence of a stable Ni-boride phase at other carbide/metal interfaces or whether the boride particles were too small or crystallographically too similar to the carbide to be detected by TEM.

Six APT specimens targeting the grain boundary were attempted on the alloy 600 CRDM nozzle #31 from North Anna 2 (NA2-N31). It was found that the metal/metal grain boundary interface typically delaminates under the high electrostatic stress applied to the APT specimen during analysis. Similar premature tip fracture behavior was observed for another heat and has been a continuing problem for some alloy 600 samples in APT analysis. Despite this difficulty, one successful run was performed of a grain boundary containing an IG Cr carbide. SEM imaging of the NA2-N31 material (Figure 27) revealed a low density of IG Cr carbides. Additionally, a higher density of smaller carbides was observed to decorate ghost grain boundaries within a given grain but have not been analyzed by APT or TEM. The APT reconstruction is displayed in Figure 27(b) using atom map images (10 nm image depth). A prominent Cr carbide is apparent, extending across the APT specimen with metal matrix from both the top (labeled 1 in the Ni map) and bottom (labeled 2 in the Ni map) grains. The Cr carbide is strongly depleted of Ni, Fe, Si, Mn and Al and weakly depleted of Ti. Visually there is apparent segregation of B and possibly P to the metal/carbide interface, although neither is present in particularly high concentrations.

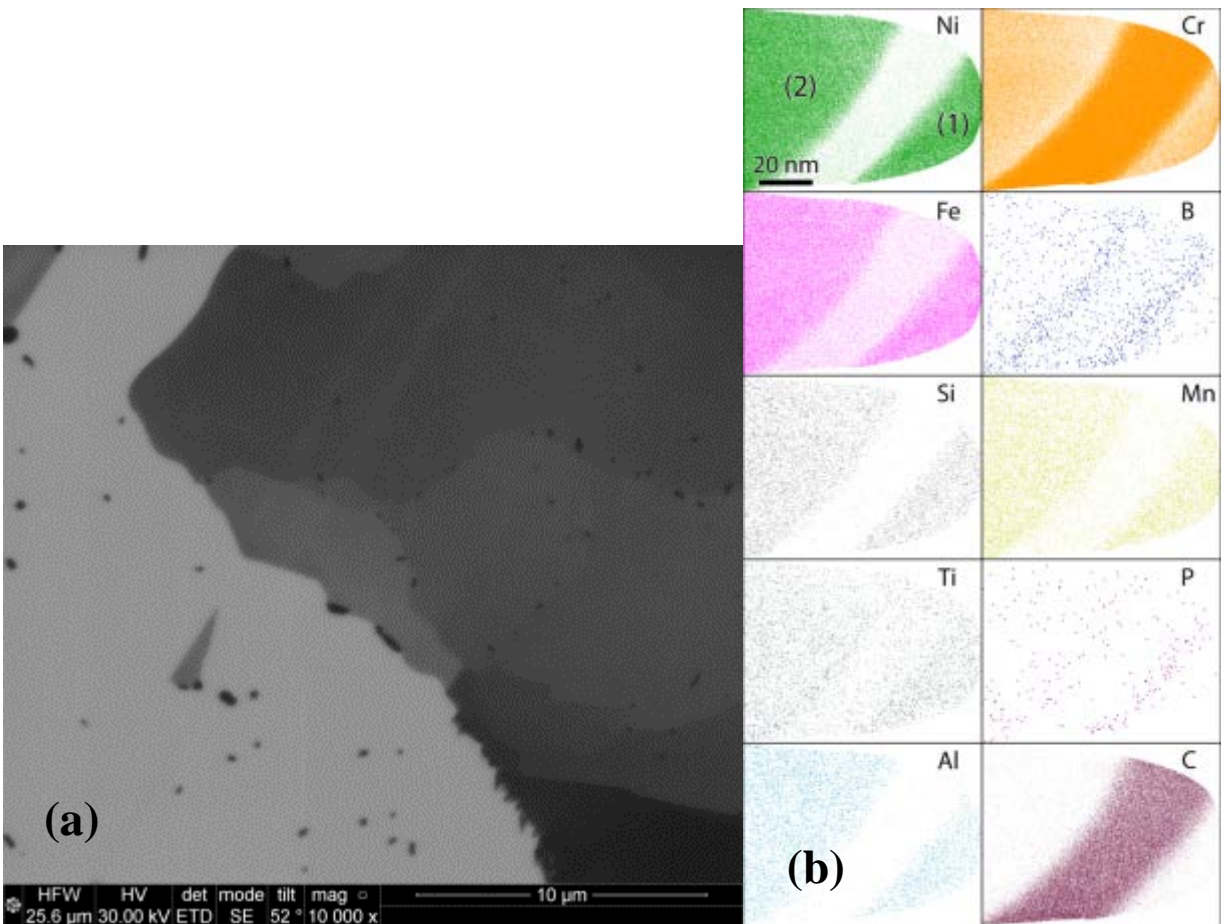


Figure 27. (a) Typical high-magnification ion-beam image of grain boundaries in the NA2-N31 alloy 600 material. A low density of IG carbides was apparent. The rough interface along the boundary in the lower right may be suggestive of cellular carbide formation. (b) APT atom maps (10 nm image depth) of an IG Cr carbide. Weak B and P segregation is apparent at the carbide/metal interface.

The composition of the Cr carbide, matrix and carbide/matrix interfaces of the NA2-N31 sample was quantified using proximity histograms (Figure 28). The Cr carbide contained small concentrations of Fe (<2 at%), Mn (<0.2 at%), Ti (~0.1 at%) and Ni (<2 at%), but is generally strongly depleted of these species compared to the matrix composition. Slight Cr depletion is apparent at each carbide/metal interface, with a minimal Cr concentration of ~10 at%. Interfacial segregation is apparent for B (~0.2 at%) and P (<0.1 at%). A slight enrichment of Fe and Ti is also present at the metal/carbide interface. In general, the observed segregation is relatively weak compared to similar interfaces in other alloy 600 materials. Because of the limited information on both the nominal alloy composition and thermal history, it is not clear whether these relatively mild interfacial segregations are a result of alloy purity or thermal treatments.

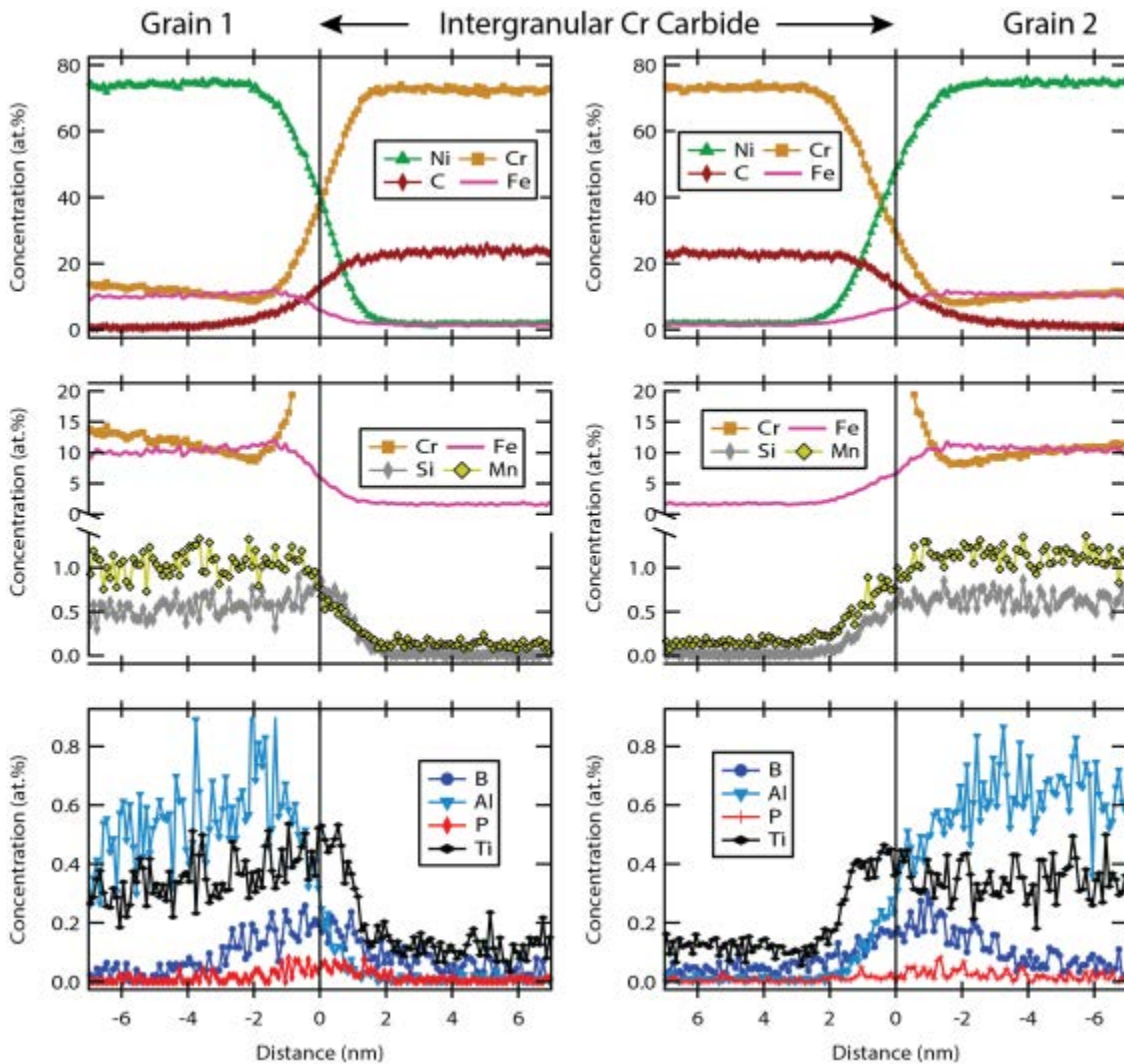


Figure 28. APT proximity histograms at the interface between the intergranular Cr carbide and (left) Grain 1 and (right) Grain 2 in Figure 20(b). The profiles quantitatively confirm the visually apparent weak segregation of B and P and also localized Cr depletion at both metal/carbide interfaces.

Grain Boundaries after Simulated PWR Primary Water Exposures

As part of research efforts within an SCC initiation project at PNNL for the DOE Office of Nuclear Energy, Light-Water Reactor Sustainability Program, many alloy 600 materials have been exposed to simulated PWR primary water to assess susceptibility to intergranular attack (IGA) and evaluate grain boundary chemistry changes associated with corrosion. Materials that were examined include CRDM nozzle #1 (M3935) from the original Davis Besse RPV head. APT analysis of this material is provided here in part because the IGA response of this material has potential relevance to understanding the SCC response, and in part because high resolution post-test examinations of the SCC test specimen crack tip areas were not funded under the NRC program. This section on IGA chemistry analysis is an excerpt from a recent conference publication [1].

Examples for two materials (Davis Besse CRDM tube heat M3935 and AREVA steam generator tube heat WF422) will be presented and discussed. Small coupons of each material were polished to a fine finish (0.05 μm silica) and suspended within stainless steel autoclaves without any applied stress. Specimens were exposed to simulated PWR primary water at 325°C for times between 100 h and 3500 h at dissolved hydrogen concentrations of 10.5 cc/kg corresponding to the Ni/NiO stability line.

TEM and APT analyses were performed on IGA in alloy 600 heat WF422 after exposure to simulated PWR primary water for 500 h and 3500 h at 325°C. SEM examinations, performed in tandem while preparing APT specimens with the dual-beam FIB, revealed that the IGA extended 0.4-1 μm after 500 h and 2-4 μm after 3500 h. A representative STEM EDS elemental map of the leading IGA in heat WF422 after the 500 h exposure is shown in Figure 29(a). Depletion of Cr, Fe and Si (and concurrent Ni enrichment) is observed both ahead of the leading IG attack and also in the adjacent metal matrix behind the leading oxidation front. In the bottom right hand corner of the panel, Ni, Cr and Fe are overlaid such that the difference in signals is shown. While there does not appear to be strong Cr signal in the Cr-K map, when overlaid on the Ni and Fe maps, the continuous Cr (green) is observed along the IGA with the increased signal suggesting local Cr_2O_3 . However, electron diffraction (not shown) was unable to prove this and identified the dominant oxide reflection as nanocrystalline MO-phase oxide. IGA wall oxides in the heat WF422 specimens commonly exhibit some crystallographic faceting into either side of the grain. The O map suggests that the attack of the adjacent grain is primarily oxide and the color map shows that the composition of the oxide is clearly Fe and Cr rich but is also non-uniform with small pockets of strong Cr enrichment.

A representative APT reconstruction of the termination of IGA in the heat WF422 sample after 500 h exposure is presented in Figure 29(b) as cross-section atom maps (10 nm image depth). The attacked grain boundary extends from the upper right to the lower left of each panel. The O signal defines the location of continuous IG oxidation that terminates just prior to the bottom of the APT specimen. Localized enrichment is apparent for Cr, Al and Fe in the oxide. Directly adjacent to the oxidation is localized depletion of Cr, Si, Al, Fe, Ti and Mn. One-dimensional concentration profiles were extracted from various site-specific locations along the IGA, as shown by isoconcentration surfaces and marked areas in Figure 30(a). The first profile (panel b) was extracted across the oxidized region marked (1) in panel (a). The oxide is enriched in Cr, but also contains a significant concentration of Ni and Fe. By comparison, the profile extracted

across region (3), which was defined by an 88 at% Cr+O isoconcentration surface (red), is more strongly Cr enriched with much less Ni and Fe. Therefore, it is reasonable to infer that this discrete region probably contains a discrete Cr_2O_3 precipitate that coincides with the oxide faceting apparent in the cross-section atom maps. Lastly, a concentration profile extracted across a non-oxidized region of grain boundary directly adjacent to the oxidation (region 3 and panel d) reveals a 20 nm wide zone of strongly altered composition, suggestive of diffusion-induced grain boundary migration as a result of IGA. Cr and Fe were depleted to trace concentrations within this broad zone (concomitant Ni enrichment), which is in good agreement with the depletion behavior observed as a result of the oxidation/sulfidation attack exhibited by the same alloy after corrosion tests by AREVA. No sulfide precipitation was detected in this specimen from our SEM, TEM or APT examinations.

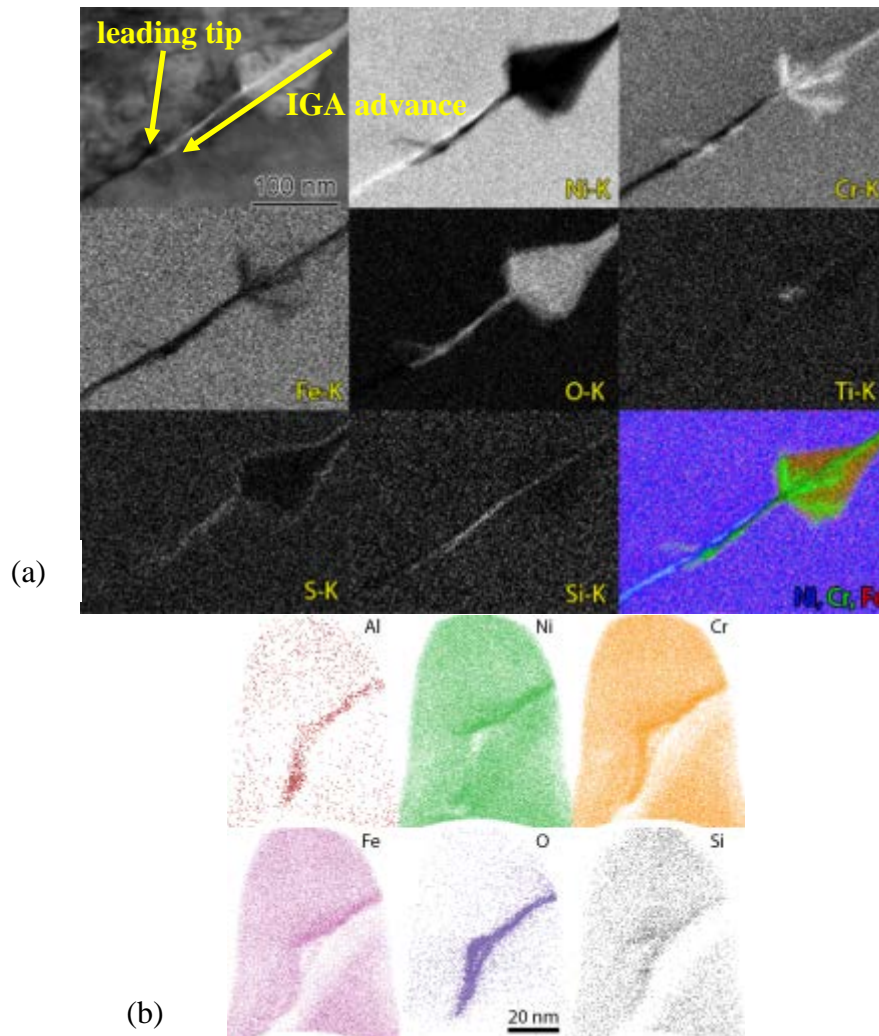


Figure 29. (a) STEM EDS elemental map of IGA in heat WF422 after exposure to simulated PWR primary water. Cr-rich oxide facets have formed with concomitant Ni enrichment and Cr depletion ahead. Electron diffraction (not shown) revealed the oxide to be comprised primarily of nanocrystalline MO-phase oxides. (b) Cross-section atom maps of the terminal IGA in heat WF422 after an additional 3000 h exposure showing Cr-rich oxides and substantial depletion of Cr, Fe and Si and grain boundary migration.

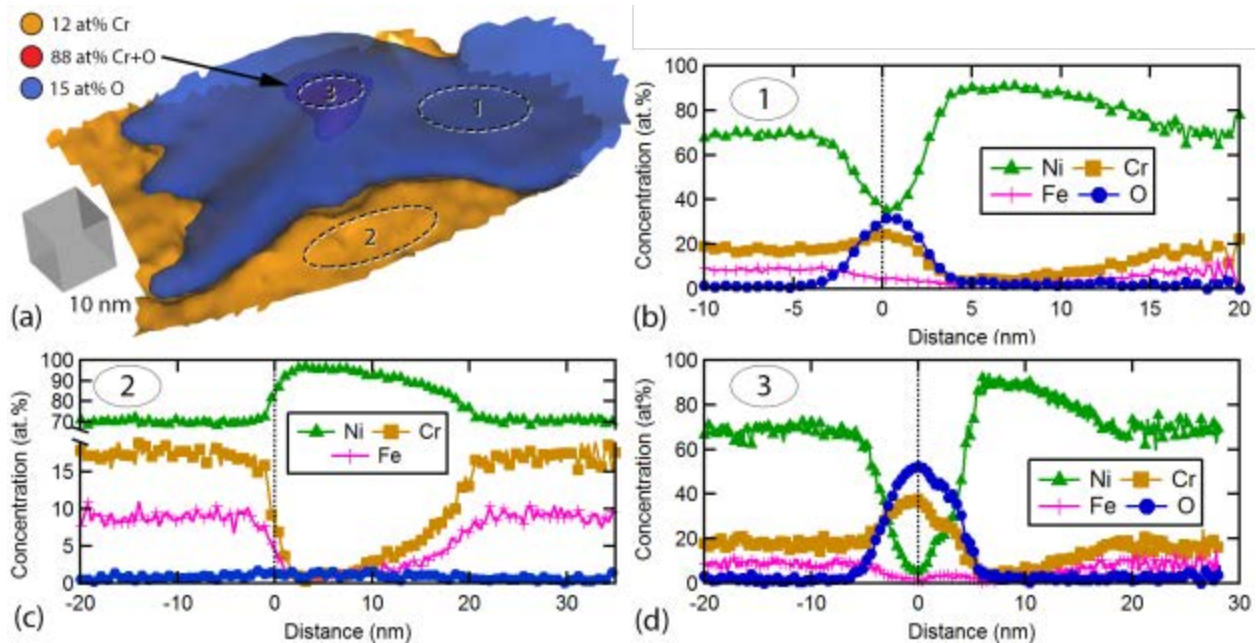


Figure 30. APT analysis of the terminal IGA of heat WF422 at 325 °C for 3500 h. (a) Isoconcentration surfaces at 15 at% O (blue) and 12 at% Cr (orange) define the oxidized region and unoxidized portions of an attacked grain boundary. An 88 at% Cr+O isoconcentration surface (red) defines a discrete Cr_2O_3 precipitate. (b)-(d) 1-D concentration profiles extracted across the indicated regions of the grain boundary. The oxide is Cr rich and Ni depleted and the surrounding metal is strongly depleted of Cr and Fe for a width of >10 nm.

APT analysis of the IGA from exposure of heat M3935 to simulated PWR primary water at 330°C for 100 h is depicted in Figure 31 as both atom maps and concentration profiles. Isoconcentration surfaces are used at 17 at% O (blue) and 8 at% Cr (orange) to define the morphology of the IGA oxide and grain boundary depletion of Cr ahead of the oxidation front. This high-B concentration alloy 600 material exhibits similar IGA characteristics to the low-B heat WF422 material. Side-by-side exposure of heat M3935 and heat WF422 for 100 h resulted in nominally identical IGA depths of ~200–500 nm with compositionally similar oxides. Oxides are Cr rich and Ni depleted with a slight Fe depletion. A Cr, Mn, Fe, Si and B depleted grain boundary exists ahead of the oxidation front, although the extent of Cr depletion (to ~4 at% Cr) is not as extreme as those found in heat WF422 (<0.5 at% Cr). Interestingly, the grain boundary also does not appear significantly migrated and strong Cr depletion is not seen in the matrix adjacent to the oxidized region. Note that a convolution exists between $^{27}\text{Al}^{16}\text{O}^+$ and $^{11}\text{B}^{16}\text{O}_2^+$ that prevents differentiation of these two species by APT. However when considering the entirety of this peak to be the BO_2 species, the maximum B concentration within the oxide is <1 at% B. This suggests that although B is strongly depleted from the grain boundary ahead of the oxidation front, it is not strongly partitioned to the IGA oxide.

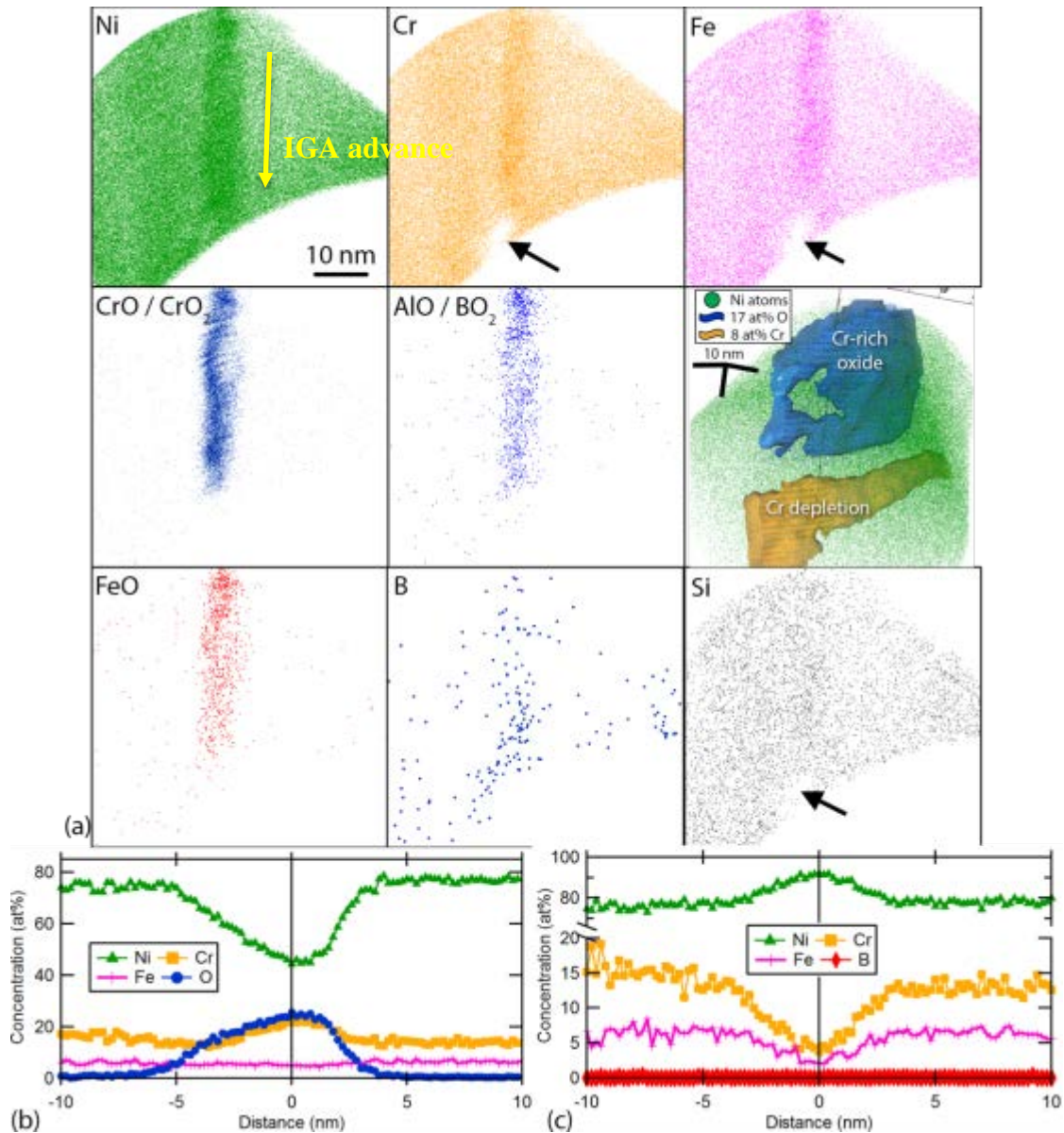


Figure 31. (a) Atom maps from the terminal IGA exhibited by alloy 600 heat M3935 after exposure to 330°C simulated PWR primary water for 100 h. Arrows indicate Cr, Fe and Si depletion ahead of the oxidation front. Isoconcentration surface at 17at% O (blue) and 8 at% Cr (orange) are used to depict the oxide morphology and zone of Cr depletion ahead of the IGA. Concentration profiles taken from (b) across and (c) ahead of the oxidation reveal a Cr-rich, Ni-depleted oxide followed by a Cr- and Fe-depleted and Ni-enriched metal. No measurable B was observed ahead of the oxidation front within the depleted zone.

The extremely high concentrations of B observed at interfaces in heats M3935 and M7929 where high SCC susceptibility has been observed in service should not be overlooked. One possible explanation for this behavior is that a critical B interfacial segregation may exist, above which SCC susceptibility is increased, but this conclusion cannot be made from our current limited analyses. The average IGA depth of heat WF422 (low B) and heat M3935 (high B) are

comparable after 100 h exposure and these two materials generally exhibit similar degradation microstructures (Cr-rich oxides with strong Cr depletion from the leading grain boundary). Boron was found to deplete from the grain boundary ahead of the IGA oxidation front, along with many other oxidizing species (Fe, Si, Mn, Ti and Al). It is important to recognize that Si is seen to segregate in alloy 600 and may act in a similar fashion as B to promote IGSCC. Further studies are needed to isolate B and Si interfacial segregation effects on susceptibility in the same alloy without significant changes in other microchemical or microstructural characteristics.

Crack-Growth Testing of Davis Besse CRDM Nozzle Materials

Crack-growth testing was conducted on 0.25T or 0.5T compact tension (CT) specimens as described earlier in this report. Environmental conditions were 325°C simulated PWR primary water (1000 ppm of boron, 2 ppm of lithium). The target dissolved hydrogen concentration was 29 cc/kg (Ni-metal stable) and was maintained for the entire test sequence on the replacement head CRDM material. Low K crack growth testing on the original head CRDM material necessitated the use of 11 cc/kg (Ni/NiO stability line where alloy 600 SCC growth peaks) to obtain DCPD-measurable crack growth rates at 15 MPa√m. Temperature was occasionally varied to evaluate the effect on SCC response, and such changes are identified in each test. Two specimens were tested in series, and as with any series loading, the stress intensity (K) can only be controlled to one of the two specimens. The stress intensity of the non-controlled specimen will only appreciably deviate from the control specimen if the crack length of the two specimens strongly diverges. SCC growth rates were investigated for stress intensity values ranging from 15 to 41 MPa√m. Specimens were first fatigue precracked in air followed by further precracking and transitioning in the high-temperature water environment. A variety of loading conditions were used to transition the TG crack front created in fatigue to an IGSCC crack.

Replacement RPV Head Alloy 600 CRDM Nozzle Heat M7929

Two 0.25T CT alloy 600 heat M7929 specimens identified at CT063 (also DB-1) and CT064 (also DB-2) were fatigue precracked in air to a length of ~0.3 mm from the notch. Aggressive cycling at 15 MHz was used first with an R of 0.3 at a K of 17.5 MPa√m, then at higher R values with a K of 20 MPa√m. The precrack length versus time plot for the CT064 specimen is shown in Figure 32 as an example of the response.

The test on CT063 and CT064 was quite complex with many phases to first properly transition from a TG fatigue crack to an IG crack where SCC growth rates could be effectively measured. An overview of the entire SCC test for the two specimens is presented in Figure 33, and a detailed step-by-step test summary is given in Table 3. Information in both the overall plot and summary table has been corrected for observed crack length obtained after post-test examinations of the crack-growth surfaces. The test on the CT063 (DB-1) specimen was ended after ~3600 hours and comprised 14 separate test phases (steps in Table 3). At that point, the CT063 specimen was removed for characterization while testing continued on the CT064 (DB-2) specimen alone until ~7800 hours and 32 test phases. Descriptions of crack growth response are provided below for important parts of the test under constant K loading to illustrate the overall results for the two heat M7929 specimens from the Davis Besse replacement head.

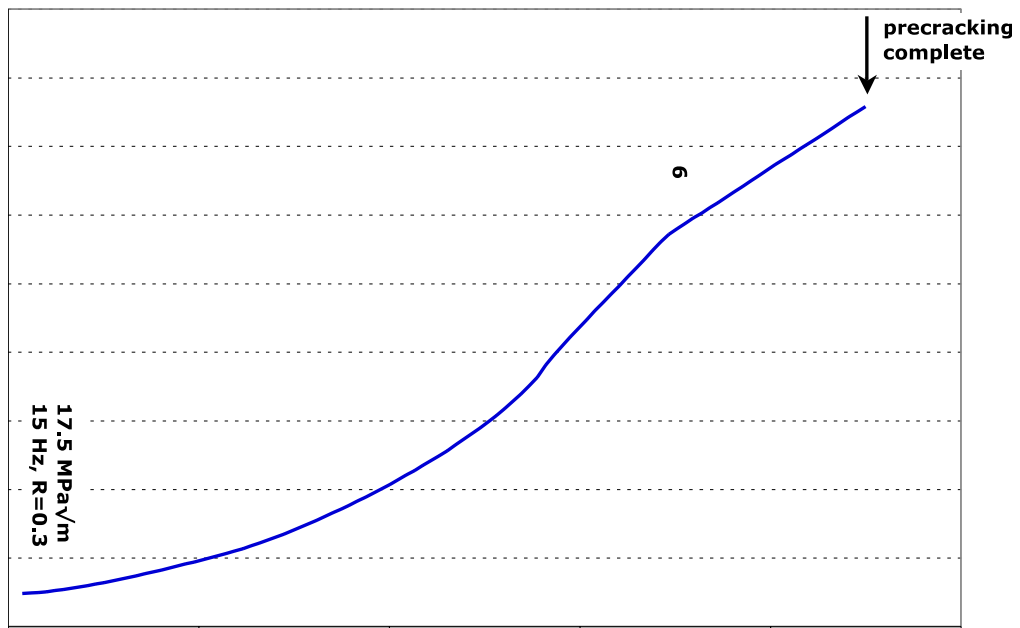


Figure 32. Air precracking response for the Davis Besse heat M7929 CT064 specimen.

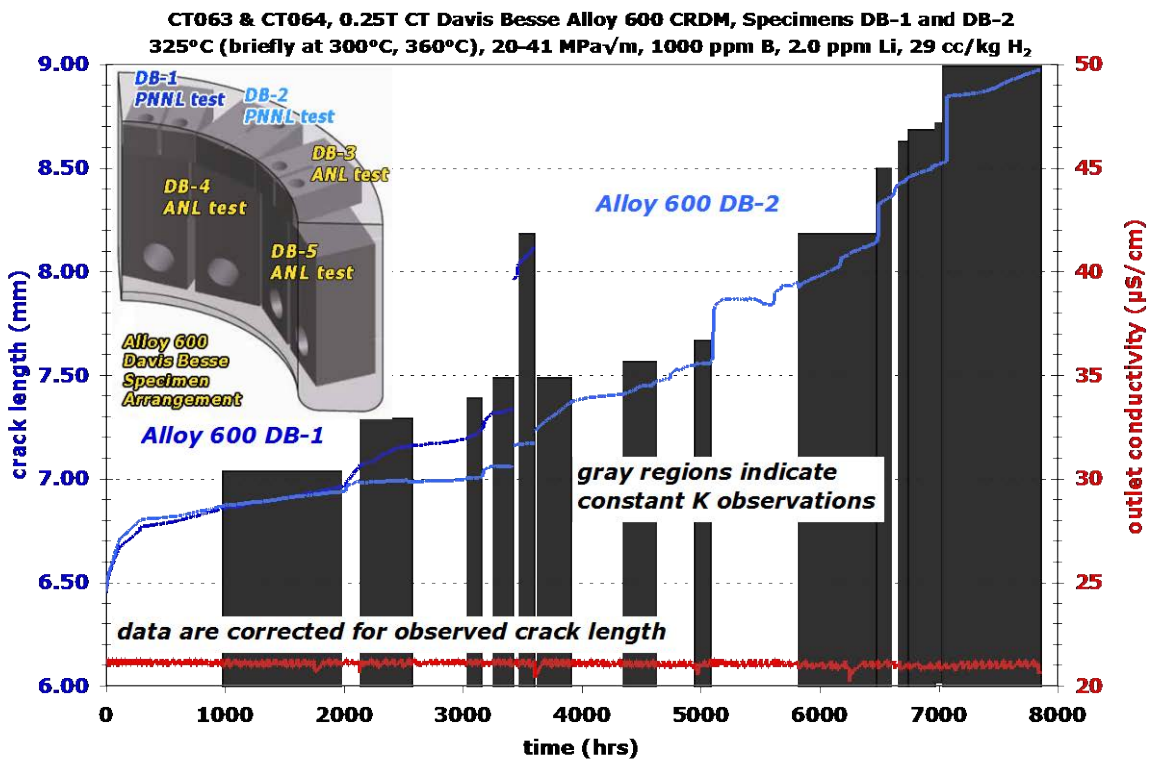


Figure 33. Corrected overview plot showing crack growth response for the Davis Besse alloy 600 specimens CT063 (DB-1) and CT064 (DB-2) in simulated PWR primary water.

Table 3. Summary of corrected data for CT063 (DB-1) and CT064 (DB-2) specimens.

Test Step	Duration (h)	R	Freq (Hz)	Hold (h)	DH (cc/kg H2)	Temp (°C)	Alloy 600 CRDM CT063 (DB-1) Heat M7929			Alloy 600 CRDM CT064 (DB-2) Heat M7929		
							S#1 Kmax (MPa \sqrt{m})	S#1 CGR (mm/s)	S#1 Approx. Crack Ext. (mm)	S#2 Kmax (MPa \sqrt{m})	S#2 CGR (mm/s)	S#2 Approx. Crack Ext. (mm)
1	9	0.5	0.1	0	10.5	325	20	1.7E-06	0.049	20	2.1E-06	0.049
2	101	0.5	0.01	0	10.5	325	20	5.0E-07	0.163	21	5.3E-07	0.191
3	170	0.5	0.001	0	10.5	325	20	1.6E-07	0.076	21	1.6E-07	0.095
4	215	0.6	0.001	2.5	29	325	21	2.0E-08	0.020	21	7.5E-09	0.015
5	528	0.5	0.001	2.5	29	325	21	4.5E-08	0.076	21	4.0E-08	0.062
6	989	---	const K	---	29	325	21	3.1E-08	0.098	21	2.1E-08	0.066
7	117	---	const K	---	65	360	21	2.0E-07	0.081	20	6.0E-08	0.024
8	403	---	const K	---	29	325	21	6.8E-08	0.090	20	1.6E-08	0.015
9	484	---	const K	---	16	300	21	1.7E-08	0.033	20	4.4E-09	0.008
10	150	---	const K	---	29	325	21	6.2E-08	0.046	20	1.0E-08	0.006
11	92	0.7	0.001	1	29	325	21	1.4E-07	0.086	19	7.3E-08	0.059
12	164	---	const K	---	29	325	21	5.1E-08	0.019	19	no growth	-0.003
13	3	0.7	0.001	2.5	29	325	21->33	not meas.	0.621	19->23	not meas.	0.103
14	183	---	const K	---	29	325	33	1.8E-07	0.162	23	1.9E-08	0.014
15	293	---	const K	---	29	325				25	1.3E-07	0.147
16	358	---	dK/dt	---	29	325				25->22	1.1E-08	0.032
17	491	---	const K	---	29	325				22	6.1E-08	0.086
18	204	0.7	0.001	1	29	325				22	6.1E-08	0.071
19	130	---	const K	---	29	325				22	no growth	0.002
20	737	---	various	---	---	325				23	not meas.	0.383
21	666	---	const K	---	29	325				30	9.6E-08	0.228
22	2	0.5	12s/12s	1	29	325				31	2 cycles	0.189
23	136	---	const K	---	29	325				31	1.0E-07	0.047
24	13	0.5	12s/12s	1	29	325				31	6.2E-07	0.037
25	15	0.5	12s/12s	2	29	325				31	3.1E-07	0.015
26	70	---	const K	---	29	325				32	6.7E-08	0.017
27	33	0.5	12s/12s	2	29	325				32	1.8E-07	0.021
28	186	---	const K	---	29	325				32	5.9E-08	0.039
29	2	0.5	12s/12s	2	29	325				32	2 cycles	0.012
30	48	---	const K	---	29	325				32	1.6E-08	0.008
31	4	---	dK/dt	---	29	325				32->41	not meas.	0.006
32	856	---	const K	---	29	325				41	6.5E-08	0.470

Transitioning from the TG precrack to an IGSCC crack over the first ~1000 hours of the test was performed at $20 \text{ MPa}\sqrt{\text{m}}$ with a load ratio of 0.5 using a systematic reduction in cyclic loading frequency. After increasing propagation rates were observed during 0.001 Hz loading with a 2.5-h hold (step 5), the test was converted to constant K with the subsequent response shown in Figure 34. After a few days, the CGRs of both specimens reached values of $\sim 2 \times 10^{-8} \text{ mm/s}$. However, DCPD measurements indicated a small increase in crack length at ~1175 h for both specimens. This bump or jump in apparent crack length was only $\sim 7 \mu\text{m}$ for DB-1 and $\sim 2.5 \mu\text{m}$ for DB-2. Review of all instrumentation records and the detail file for the test (updated approximately once per minute) did not reveal any change in system conditions or a load fluctuation to explain the increase. Both specimens again exhibited the same propagation rates as before the event. Close examination of other constant K observations revealed several additional small jumps in the crack length suggesting that there were ligaments or contact points forming and breaking during the constant K exposure. Constant K evaluation at this 325°C , 29 cc/kg H_2 condition (step 6) was continued for ~1000 hours with corrected SCC rates of 3.1 and $2.1 \times 10^{-8} \text{ mm/s}$ for CT063 (DB-1) and CT064 (DB-2), respectively.

After the SCC growth rate was documented at 325°C , the influence of temperature was evaluated by first increasing temperature to 360°C while maintaining a constant offset in the corrosion potential with respect to the corrosion potential at the Ni/NiO stability line (Figure 35). CGRs increased to 2.0×10^{-7} and $6.0 \times 10^{-8} \text{ mm/s}$ with at least one apparent crack length jump in the faster growing DB-1 specimen.

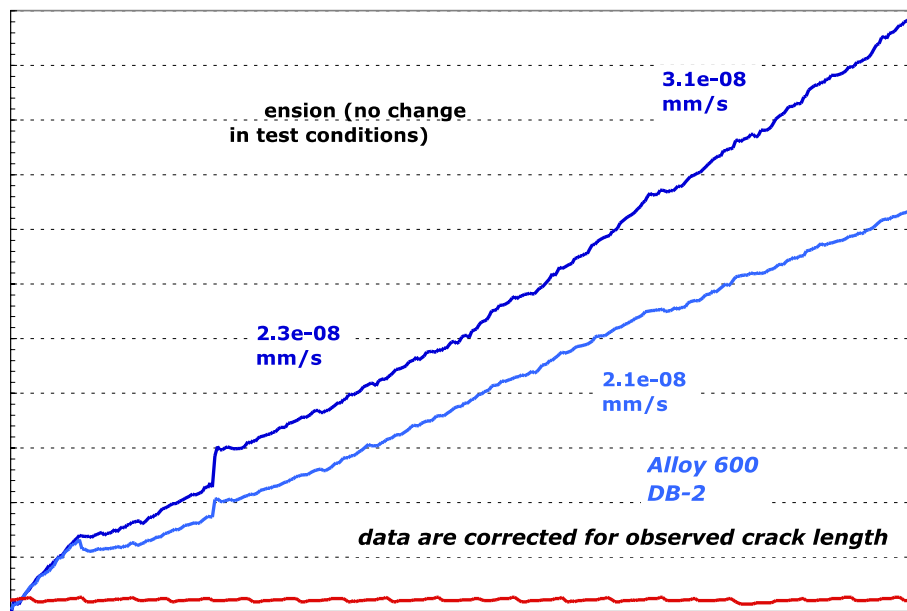


Figure 34. Crack-growth response at constant K in 325°C PWR primary water for the Davis Besse alloy 600 specimens CT063 (DB-1) and CT064 (DB-2).

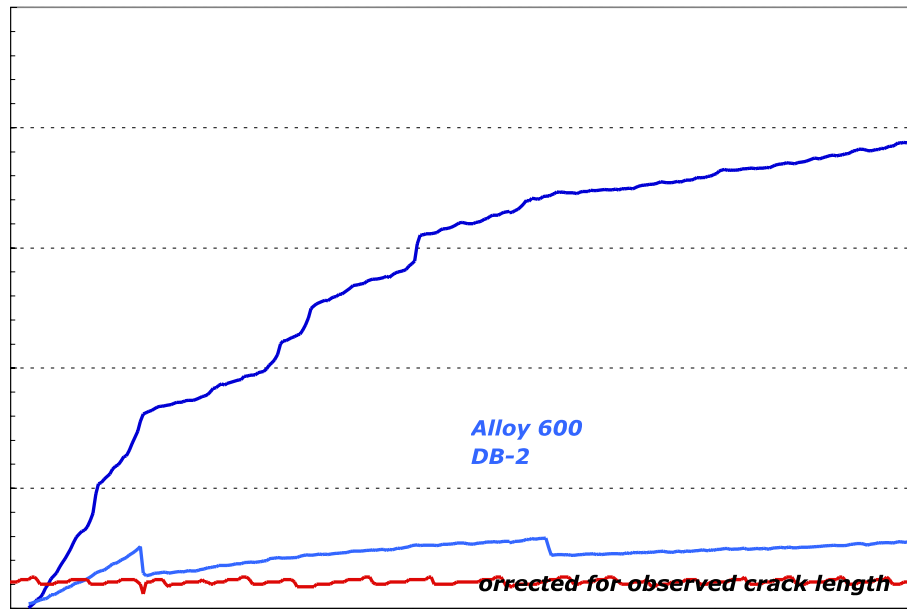


Figure 35. Measured SCC growth response as a function of test temperature in the Ni metal stability regime with ECP held at the same offset relative to the Ni/NiO stability line.

Upon returning to 325°C in step 8 (at ~2100 h), the CGR was ~2X higher at 6.8×10^{-8} mm/s for the DB-1 specimen than measured for the prior exposure at 325°C (step 6). The DB-2 specimen, however, returned to almost the same value. As documented in Table 3, two additional constant K evaluations were performed at 325°C and 29 cc/kg H₂ in steps 10 and 12 separated by a brief cycle + hold loading. The SCC growth rates remained at $5-7 \times 10^{-8}$ mm/s. Once again, jumps were seen in the crack length for the CT063 (DB-1) specimen during the constant K exposures. Exposure at 300°C produced stable, constant K crack growth in both specimens. Temperature effects on the measured SCC growth rates are summarized in Figure 36 showing a consistent increase in propagation rates with increasing temperature. An activation energy of ~125-130 kJ/mole is indicated.

The decision was made to evaluate a slightly higher K values and dK/da loading was applied in step 13 increasing the K from 21 to 33 MPa√m for the DB-1 specimen under the same 325°C PWR primary water conditions. Another attempt was made to measure a SCC growth rate at constant K in step 14 and resulted in rapid propagation for the CT063 (DB-1) specimen with a growth rate of $\sim 1.8 \times 10^{-7}$ mm/s (Figure 37). The dK/da ramp produced a much smaller increase in K from 19 to 23 MPa√m for the CT064 (DB-2) specimen and produced an SCC growth rate of 1.9×10^{-8} mm/s in step 14 similar to what was measured in previous 325°C constant K evaluations during steps 6, 8 and 10. As a result of the much faster propagation rates for the CT063 (DB-1) specimen, the test was shut down at ~3600 hours and CT063 specimen was removed for characterizations of the crack profile and the crack growth surfaces.

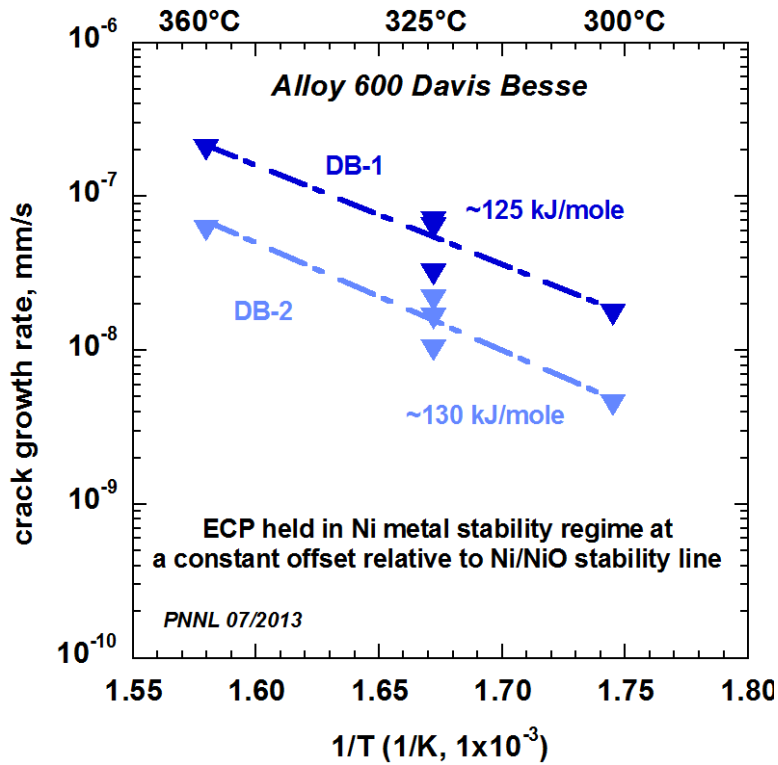


Figure 36. Temperature effect on SCC growth rate at 20 MPa \sqrt{m} for the Davis Besse alloy 600 CRDM specimens CT063 (DB-1) and CT064 (DB-2).

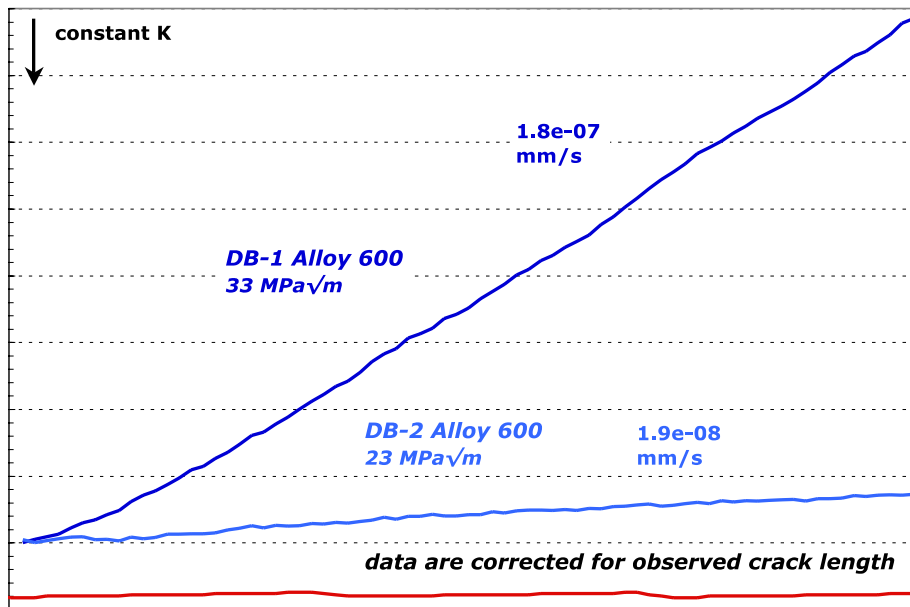


Figure 37. Constant K crack-growth response at a higher K level for the CT063 (DB-1) and the CT064 (DB-2) specimens in 325°C simulated PWR primary water.

After examination of the crack length in the side grooves by optical and SEM techniques, the CT064 (DB-2) specimen was remounted and test conditions were reestablished at 325°C in simulated PWR primary water with a slightly higher K value of 25 MPa√m. Somewhat unexpectedly, the initial constant K propagation rate in step 15 was 1.3×10^{-7} mm/s as shown in Figure 38. This rate is approximately an order of magnitude faster than observed previously for this specimen and a negative dK/da was applied in step 16 decreasing the K value to 22 MPa√m. Constant K growth rates were found to drop to 6.1×10^{-8} mm/s, but then the crack propagation appeared to stall requiring several different loading condition changes to resolve including increasing the K to 30 MPa√m in step 20. As a result of these transitioning steps, more rapid SCC growth was again observed at constant K in step 21. However as documented in Figure 39, the crack growth continued to show a tendency to slow down with time and occasional crack jumps were observed during constant K loading. A very brief periodic unload consisting of 2 cycles prompted a large jump in crack length of ~0.2 mm indicating ligaments and/or contacts were present behind the crack front resulting in an under prediction of the crack length by DCPD. Taking into account these crack length jumps, the best estimate for the SCC growth rate in Figure 39 is $\sim 1.7 \times 10^{-7}$ mm/s. This is consistent with the observation at 25 MPa√m shown in Figure 38. Difficulties in obtaining stable crack growth persisted throughout the remainder of the test and a significant increase in K (to 41 MPa√m) was produced in step 31 and a final constant K evaluation indicated an SCC propagation rate of $\sim 6.5 \times 10^{-8}$ mm/s. The test was then ended and the CT064 specimen was sectioned for side-surface crack profile examination while the remaining piece was fatigue fractured in air for characterization of the crack-growth surface.

Constant K crack-growth results for the replacement head alloy 600 nozzle heat M7929 specimens CT063 (DB-1) and CT064 (DB-2) are summarized in Figure 40. The measured SCC propagation rates do slightly increase with the K level and the maximum rate observed was 1.8×10^{-7} mm/s. All data fall below the MRP-55 95% bounding disposition curve with most points between the 50% and 75% bounding curves.

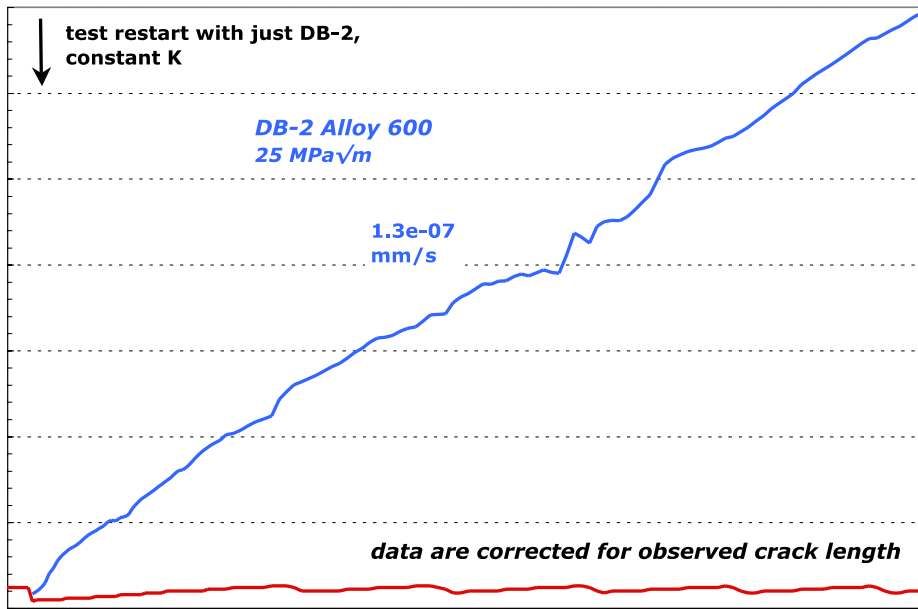


Figure 38. Constant K crack-growth response for Davis Besse specimen CT064 (DB-2) after test restart in 325°C simulated PWR primary water.

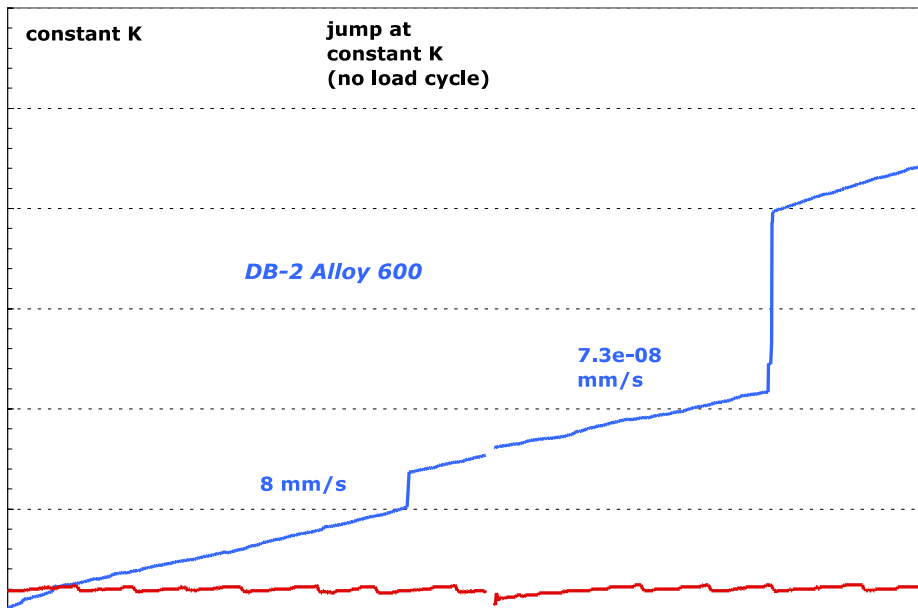


Figure 39. Constant K crack-growth response in steps 21-23 for Davis Besse specimen CT064 (DB-2) in 325°C simulated PWR primary water.

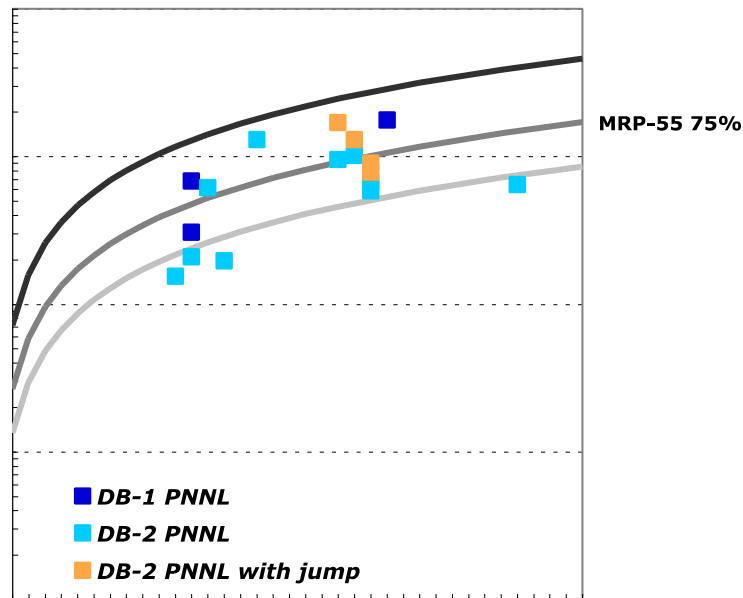


Figure 40. Corrected crack growth rate versus K plot for Davis Besse alloy 600 specimens CT063 (DB-1) and CT064 (DB-2) tested at PNNL.

Original RPV Head Alloy 600 CRDM Nozzle Heat M3935

SCC studies were also performed on nozzle #1 from the original Davis Besse RPV head. This nozzle was made from alloy 600 heat M3935 and is the same heat of alloy 600 used to make nozzle #3 that was tested by ANL with results reported in NUREG/CR-6921. CGR testing was initiated on specimens from the 90 degree (specimen CT090, H1N1 #1) and 270 degree (specimen CT091, H1N1 #2) positions as indicated by the cut plan in Figure 2. The simulated PWR primary water environment was set to 325°C, 29 cc/kg dissolved hydrogen (Ni-metal stable), 1000 ppm B and 2 ppm Li. The initial stress intensity was set to a low value of 15 MPa√m with the intent of getting a more complete evaluation of K effects on SCC CGRs. An overview of the entire test is shown in Figure 41, and a summary of data is listed in Table 4.

As shown in Figure 41 and Table 4, early testing at low K (15 MPa√m) with a dissolved hydrogen concentration of 29 cc/kg (Ni metal stable ECP) resulted in a decreasing DCPD crack length with time under constant K conditions. Various cyclic and cycle + hold loading steps were employed, but the apparent crack length was observed to decrease even during some cycle + hold loading steps. This is believed to be due to Ni metal bridge formation in the tight cracks, and electrochemical conditions were switched to the Ni/NiO stability line by dropping the dissolved hydrogen concentration to 11 cc/kg at a test time of ~1550 hours. Testing at PNNL and other labs at higher K levels have shown that moving from 29 cc/kg in the Ni metal stability regime to 11 cc/kg at the Ni/NiO stability line can increase the CGR by a factor of ~2x [2,3].

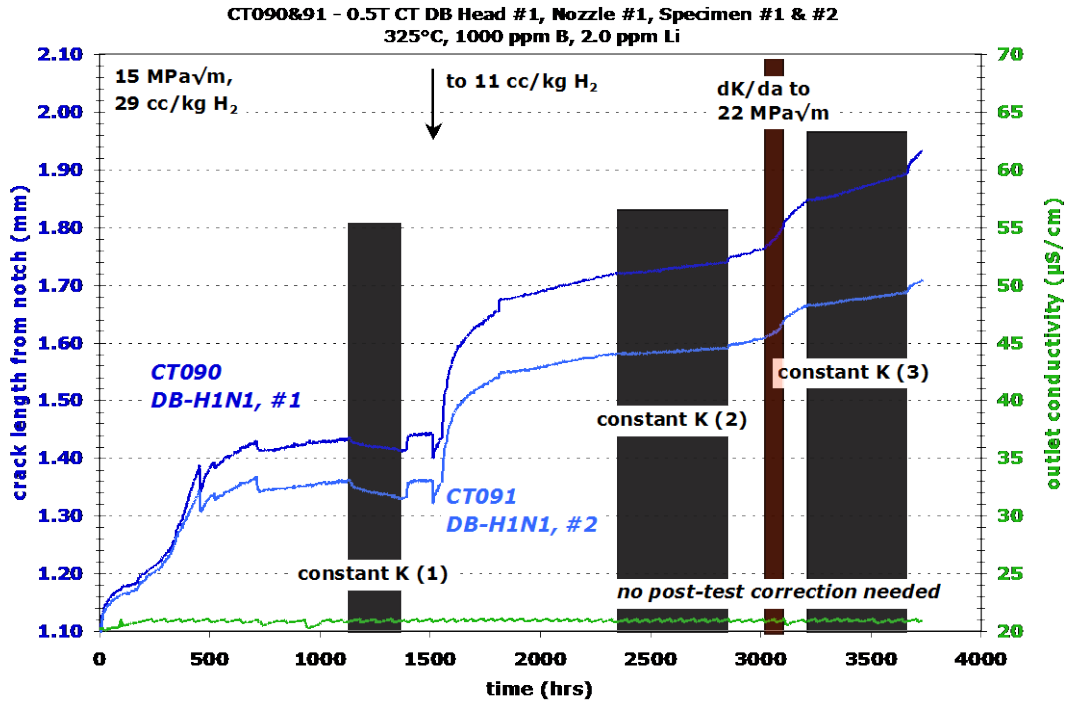


Figure 41. Overview plot showing crack growth response for the Davis Besse alloy 600 specimens CT090 (H1N1 #1) and CT091 (H1N1 #2) in simulated PWR primary water.

Constant K crack growth response was finally determined at a low K value of 15 MPa√m in step 11 as documented in Figure 42. Stable CGRs of 1.3×10^{-8} mm/s and 6.9×10^{-9} mm/s were obtained for the #1 and #2 specimens, respectively. After maintaining constant K for ~510 hours and accumulating a DCPD-indicated ~20 µm and 10 µm, respectively, cycle + hold conditions were re-established and an immediate jump in the DCPD-measured crack lengths occurred. These jumps of 5-10 µm are relatively minor, and the effect on the constant K CGRs was also minor (~20%) with specimen #1 corrected to $\sim 1.5 \times 10^{-8}$ mm/s and specimen #2 to $\sim 8.7 \times 10^{-9}$ mm/s. K was then increased to 22 MPa√m by dK/da during cycle + hold loading in step 13.

Table 4. Summary of Corrected Data for CT090 (H1N1 #1) and CT091 (H1N1 #2) Specimens

Test Step	Duration (h)	R	Freq (Hz)	Hold (h)	DH (cc/kg H2)	Temp (°C)	Alloy 600 CRDM H1N1 #1 M3935			Alloy 600 CRDM H1N1 #1 M3935		
							S#1 Kmax (MPa√m)	S#1 CGR (mm/s)	S#1 Approx. Crack Ext. (mm)	S#2 Kmax (MPa√m)	S#2 CGR (mm/s)	S#2 Approx. Crack Ext. (mm)
1	163	0.5	80s/20s	0	29	325	15	4.2E-08	0.074	15	4.2E-08	0.078
2	288	0.5	0.1	0	29	325	15	3.0E-07	0.226	15	2.4E-07	0.196
3	69	0.5	230s/20s	0	29	325	15	--	0.000	15	--	0.000
4	194	0.5	480s/20s	0	29	325	15	6.5E-08	0.036	15	4.8E-08	0.0032
5	405	0.5	480s/20s	2.5	29	325	15	1.7E-08	0.020	15	1.2E-08	0.016
6	270	---	const K	---	29	325	15	--	0.000	15	--	0.000
7	118	0.5	480s/20s	2.5	29	325	15	--	0.000	15	--	0.000
8	44	0.5	480s/20s	0	29	325	15	--	0.000	15	--	0.000
9	258	0.5	480s/20s	0	11	325	15	7.4E-08	0.022	15	6.5E-08	0.019
10	500	0.5	480s/20s	2.5	11	325	15	2.4E-08	0.041	15	1.8E-08	0.022
11	551	---	const K	---	11	325	15	1.5E-08	0.029	15	8.7E-09	0.016
12	50	0.5	480s/20s	2.5	11	325	15	--	0.011	15	--	0.010
13	210	0.5	480s/20s	2.5	11	325	15-22	--	0.062	15-22	--	0.041
14	91	0.5	480s/20s	2.5	11	325	22	1.0E-07	0.040	22	6.7E-08	0.020
15	554	---	const K	---	11	325	22	3.8E-08	0.061	22	1.6E-08	0.034
16	66	0.5	480s/20s	2.5	11	325	22	1.1E-07	0.039	22	4.4E-08	0.024

Constant K crack growth response was determined at this higher K value as documented in Figure 43. Stable CGRs of 3.2×10^{-8} mm/s and 1.6×10^{-8} mm/s were obtained for the #1 and #2 specimens, respectively. After maintaining at constant K for ~470 hours and accumulating a DCPD-indicated length change of ~50 μm and ~25 μm, cycle + hold conditions were re-established and an immediate jump in the DCPD-measured crack lengths occurred. The jumps represent a relatively minor crack length increase of 5-15 μm, and the effect on the constant K CGRs was small with specimen #1 corrected to 3.8×10^{-8} mm/s and specimen #2 to 1.9×10^{-8} mm/s. These SCC CGRs measured at 22 MPa√m are ~3X higher than those determined at 15 MPa√m. The decision was made to end this test and quantify the data after post-test characterizations as described in the next section.

The DCPD-measured crack length of the CT090 and CT091 specimens was found to accurately represent the actual crack length, and no post-test correction to crack length or stress intensity was needed. The overall summary of the PNNL constant K CGR versus K plot for both the original head and replacement head CRDM nozzles is shown in Figure 44. In general, the CRDM material from the original head trends slightly below that of the CRDM material from the replacement head.

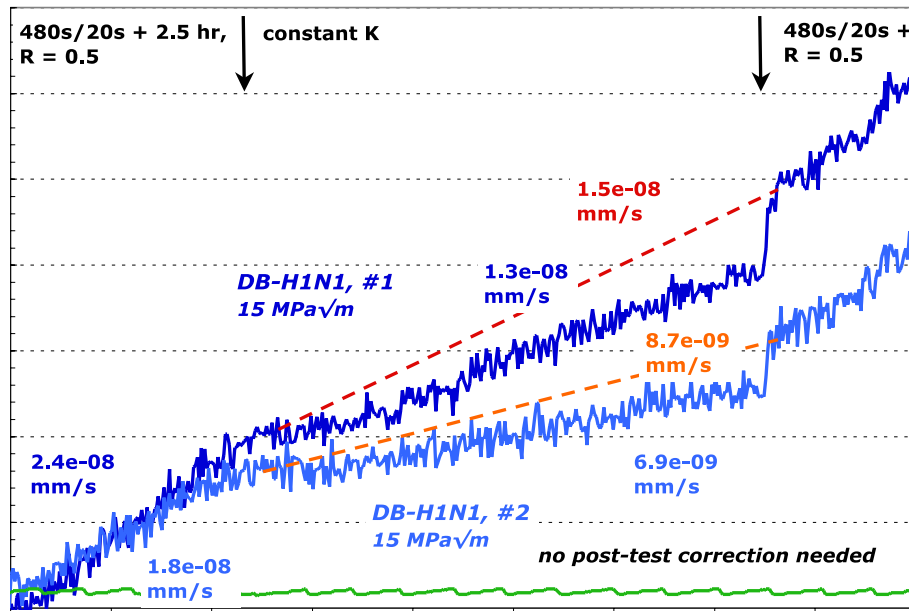


Figure 42. Constant K crack growth response of CT090 (H1N1 #1) and CT091 (H1N1 #2) in simulated PWR primary water.

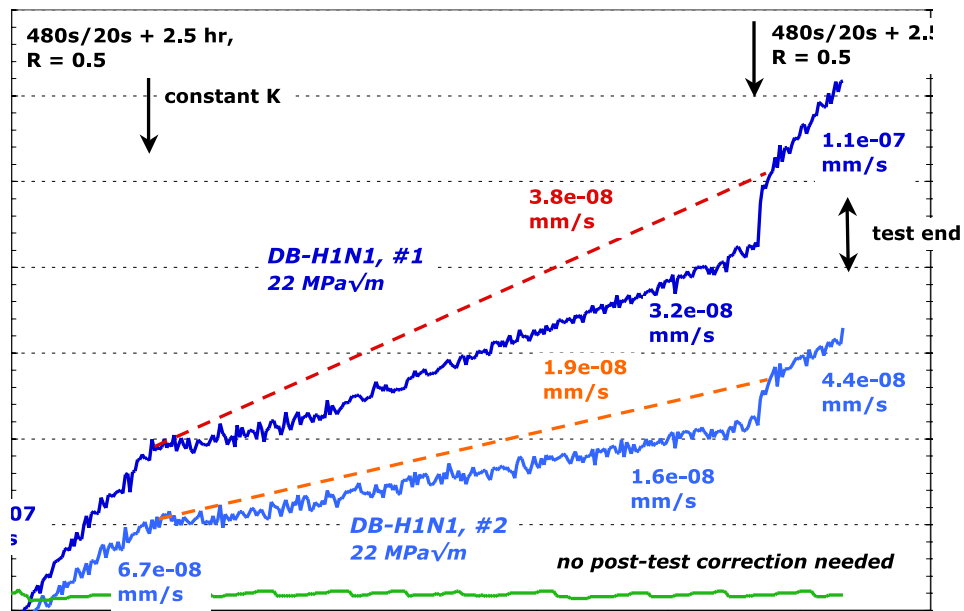


Figure 43. Final constant K crack growth response of CT090 (H1N1 #1) and CT091 (H1N1 #2) in simulated PWR primary water at the higher K level of 22 MPa√m.

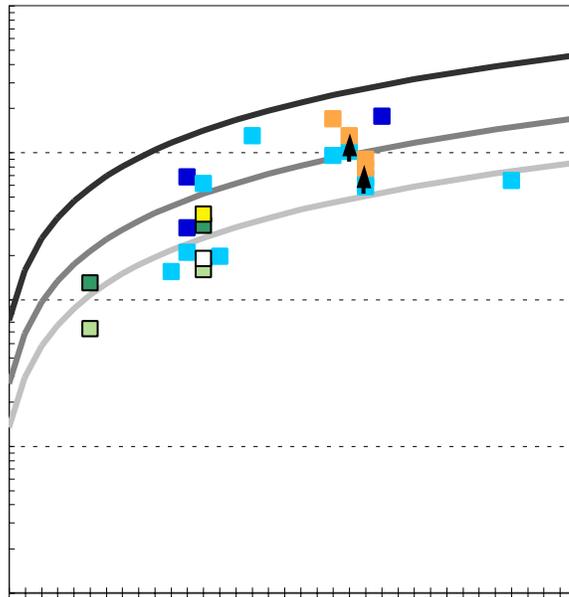


Figure 44. Constant K CGR versus stress intensity for the M3935 (DB-H1N1 #1, #2) and M7929 (DB-1, DB-2) Davis Besse CRDM materials removed from service.

Post Test Characterizations

Replacement RPV Head Alloy 600 CRDM Nozzle #4 Heat M7929

After SCC testing, the 0.25T specimens were sliced into an ~2 mm wide piece that was polished to a colloidal silica finish (better than 1 μm finish) for cross section characterization while the remaining thicker piece was fatigued open for crack growth surface characterization. Observation of the crack growth surfaces revealed 100% IG engagement across the width of the sections as illustrated for the CT063 DB-1 specimen shown in Figure 45. Extensive branch cracking was also found. Measurements of crack extension on the crack growth surface revealed that during SCC testing, the overall DCPD-measured crack length was only 10% less than actual crack length. A similarly good correlation between DCPD and actual crack length was found for the CT064 DB-2 specimen.

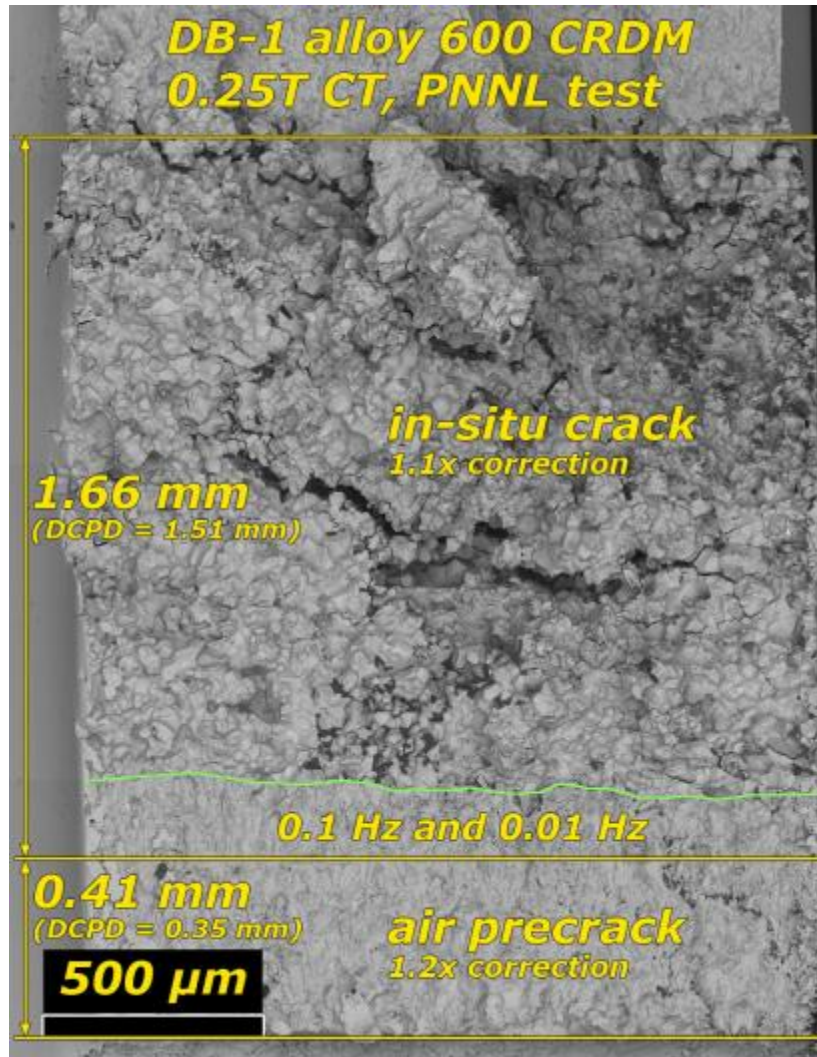


Figure 45. SEM-SE image of the crack growth surface of CT063 (DB-1) replacement head CRDM nozzle.

Cross section SEM BSE images of the CT063 (DB-1) specimen shown in Figures 46-48 reveal a relatively open main crack and as with the crack *surface* image, a large number of branch cracks. The crack was surprisingly open for having experienced a peak stress intensity of only 33 MPa√m. While some of the branch cracks are fairly open, many of the branch cracks are very tight as shown in Figures 47 and 48. An optical image in Figure 49 of the crack side surface of the CT064 (DB-2) specimen reveals a similar crack morphology.

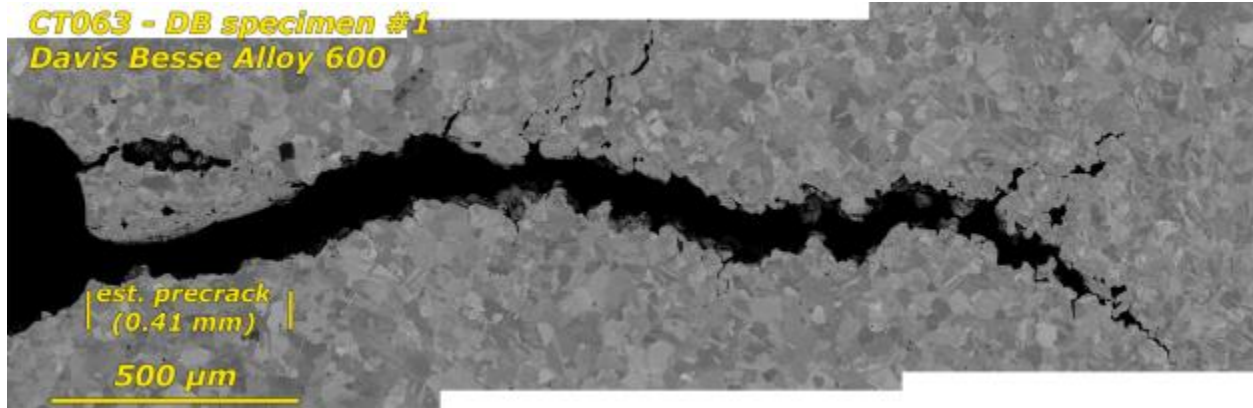


Figure 46. SEM-BSE image the crack cross section of the CT063 (DB-1) specimen.

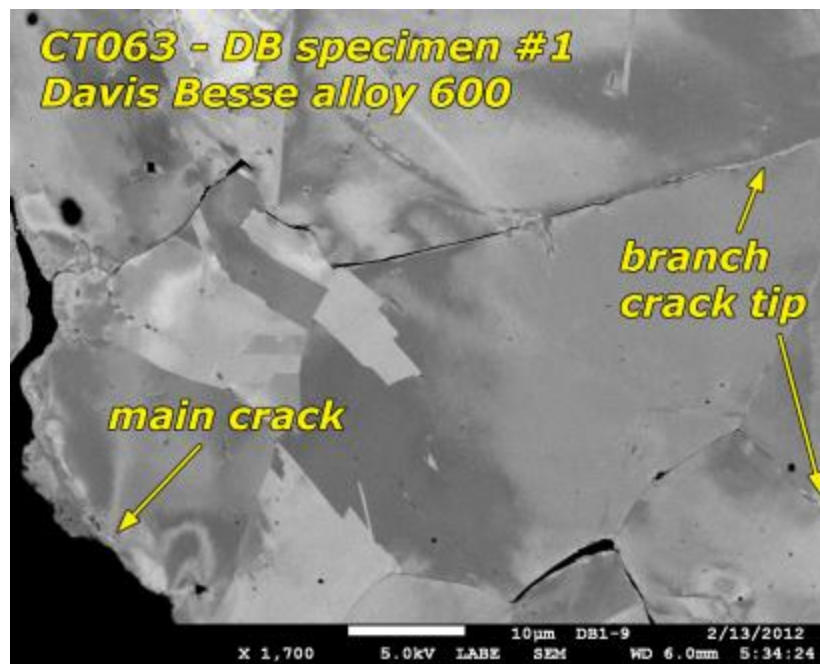


Figure 47. SEM-BSE crack cross section image of CT063 (DB-1) showing tight branch cracks.

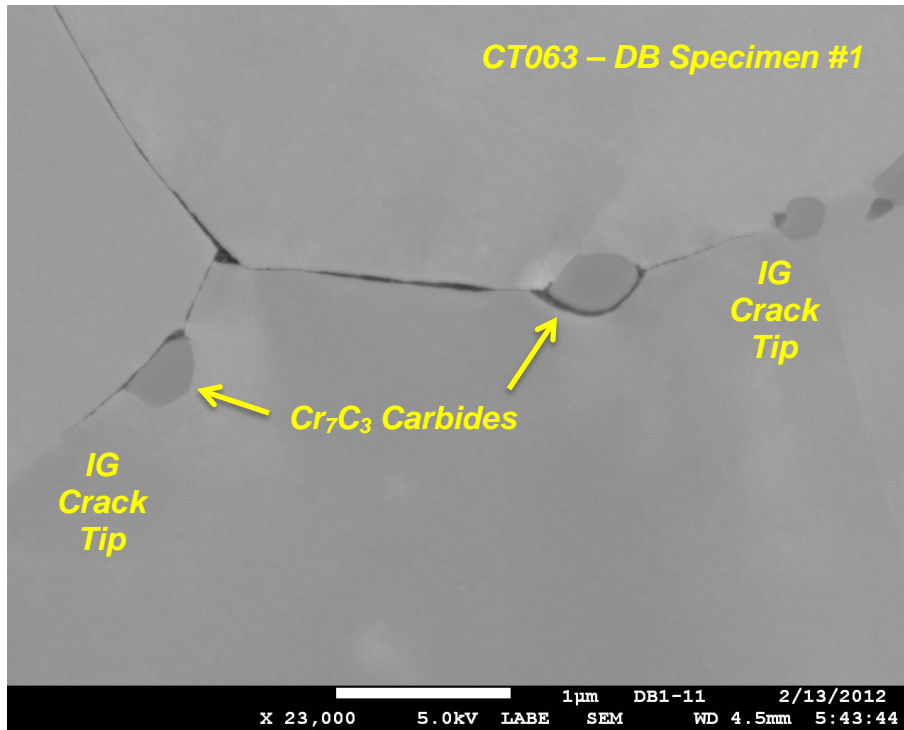


Figure 48. Higher magnification SEM-BSE crack cross section image of CT063 (DB-1) showing tight, branched cracks on grain boundaries with carbides.

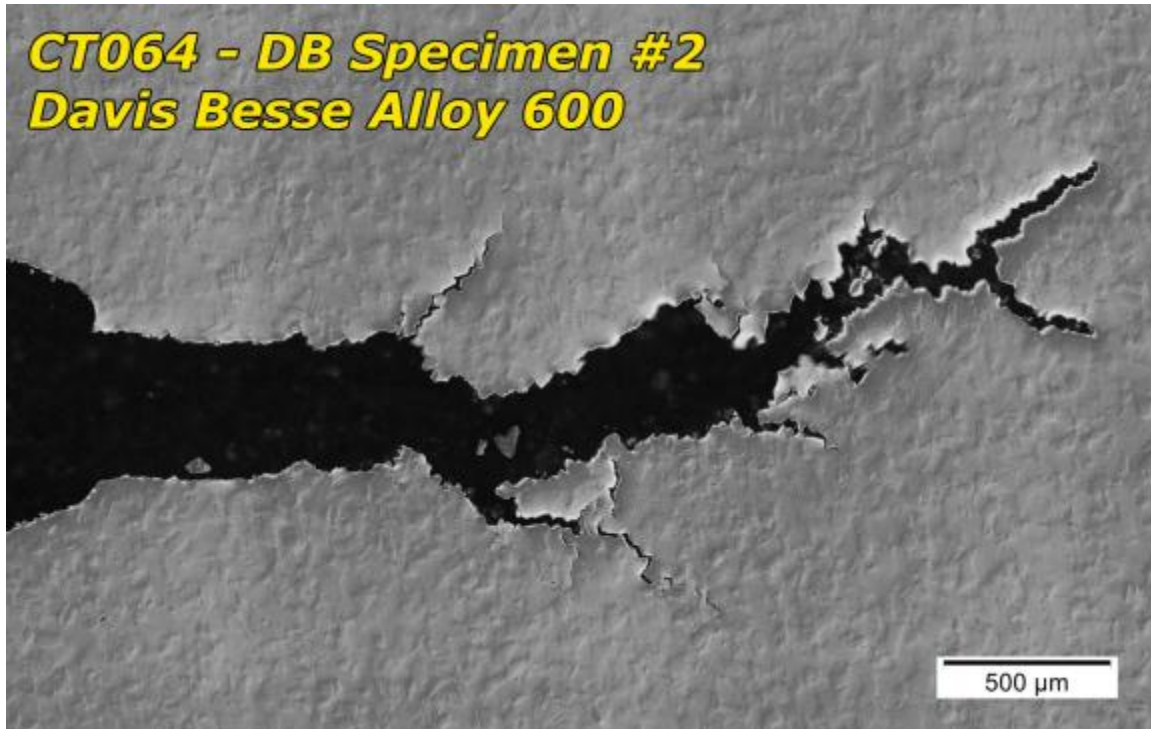


Figure 49. Optical image of the crack cross section of the CT064 (DB-2) specimen. Significant branching is apparent.

Original RPV Head Alloy 600 CRDM Nozzle #1 Heat M3935

As with the 0.25T CT specimens, these 0.5T CT specimens were cut into a slice for crack profile imaging (about 4 mm wide) and a slice for crack surface imaging (about 8 mm wide). Optical images of the crack growth surface of the two CT specimens (CT090 and CT091) cut from nozzle #1 of the original RPV head are shown in Figures 50 and 51. Yellow lines indicate the extent of air precrack and the final crack front. The large grain size of this material is readily apparent with grain sizes approaching 0.5 mm across the entire width of this section of the image. The DCPD-measured in situ crack length of 0.61 mm of the CT091 specimen (crack growth plot in Figure 41) is in excellent agreement with the measured average in situ crack length of 0.67 mm on the ~8 mm wide portion of the CT091 specimen (Figure 51). The DCPD-measured in situ crack length of 0.84 mm for the CT090 specimen is approximately 20% higher than the measured average in situ crack extension (Figure 50), but without knowledge of the crack extension in the 4 mm wide piece that was used for cross section imaging, a 20% difference is not considered worth correcting.

Cross section images of the two specimens are shown in Figures 52-54. For these specimens where K was no higher than $22 \text{ MPa}\sqrt{\text{m}}$, the main crack is very tight. The appearance of the crack growth surfaces in Figures 50 and 51 suggest that the specimens transitioned to IG cracking starting from the air precrack. Examination of the cross section images reveal that IG cracking did indeed start directly from the air precrack, but rather than starting from the tip of the TG air precrack, the IGSCC cracking started from grain boundaries that intersected the air precrack. Extensive crack branching is indicated by the cross section images.



Figure 50. Optical image of the crack growth surface of CT090 - DB-H1N1 #1 (M3935). The yellow lines indicate the air precrack and final crack front locations. Note IG facets illustrating large grain sizes of ~0.5 mm in diameter.



Figure 51. Optical image of the crack growth surface of CT091 - DB-H1N1 #2 (M3935). The yellow lines indicate the air precrack and final crack front locations.

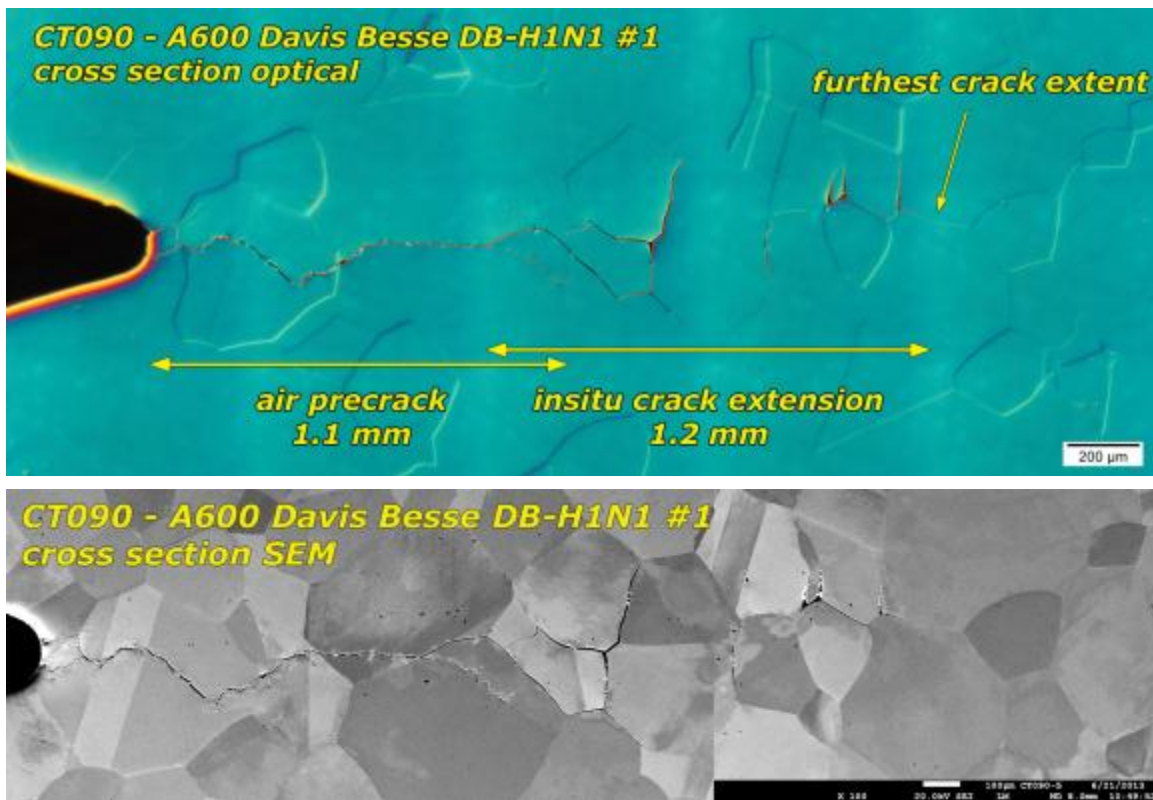


Figure 52. Optical (top) and SEM-SE (bottom) images of crack profile from side surface cross-section sample for CT090 (H1N1 #1) M3935 specimen.

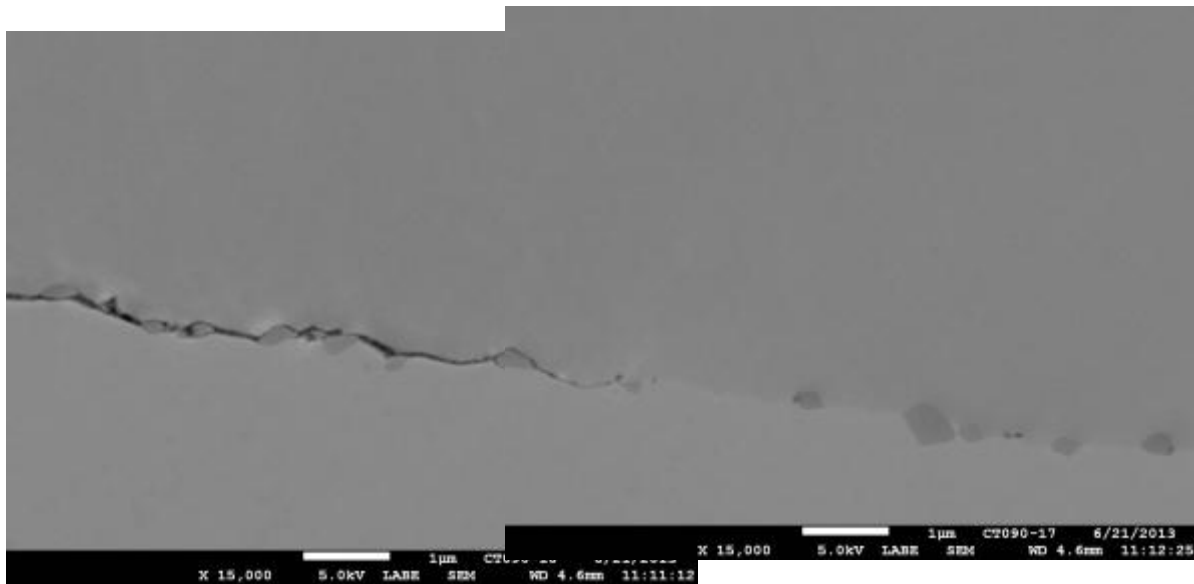


Figure 53. SEM-BSE images showing the IG crack tip in the CT090 specimen (M3935).

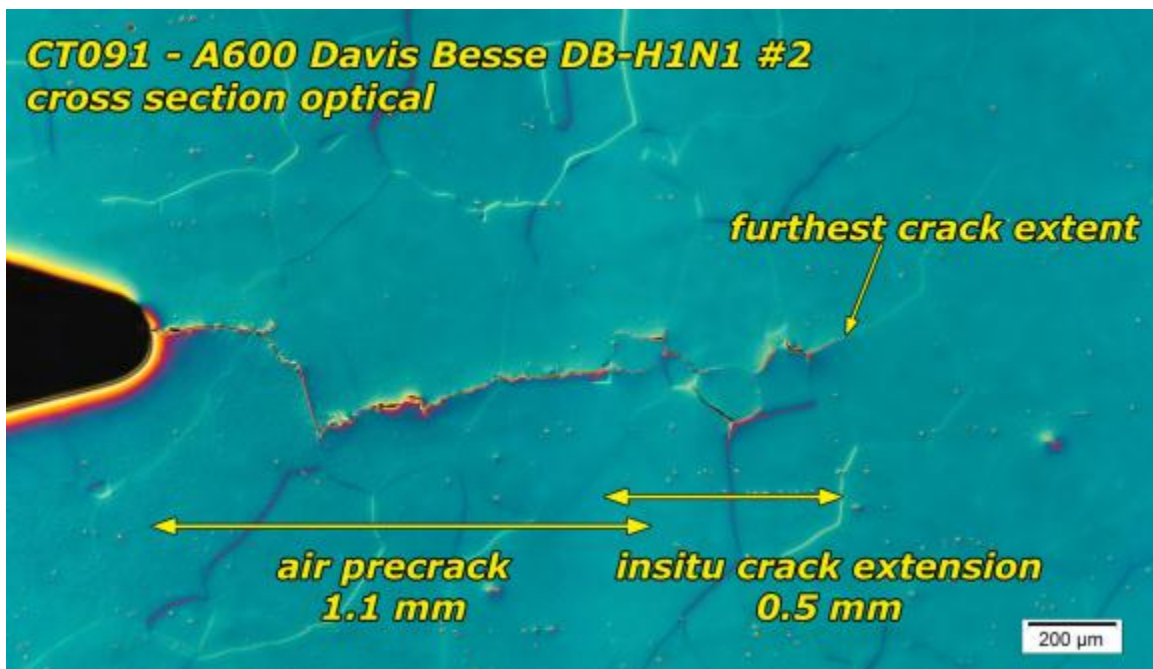


Figure 54. Optical image of crack profile of the CT091 (H1N1 #2) specimen (M3935).

Discussion

The dissolved hydrogen concentration and the electrochemical potential (ECP) with respect to the Ni/NiO stability line does affect the SCC response of alloy 600 in PWR primary water. Therefore, the difference in dissolved hydrogen content between the replacement head tests (29 cc/kg, Ni-metal stable) and the original head tests (11 cc/kg, at Ni/NiO stability line) must be considered. Morton's [2] and Andresen's data [3] indicate that testing at the Ni/NiO stability line (11 cc/kg H₂) will produce an approximate 2x higher CGR compared to Ni metal stable conditions at 29 cc/kg. Application of this factor to the crack growth response of the two CRDM heats of alloy 600 suggests that the replacement head nozzle material (DB-1, DB-2) has a higher SCC susceptibility as shown in Figure 55 where the CGRs of the original head material have been reduced by a factor of 2x due to testing at 11 cc/kg H₂. The original head CRDM material CGRs now lie at or below the 50% bounding line in MRP-55, while the replacement head CRDM material trends on the 75% bounding line. This difference in CGR response is generally consistent with lifetimes of the original and replacement head CRDM materials, respectively. However, further testing would be needed to fully assess this possible effect of dissolved hydrogen on the results. Regardless of the difference in CGR between the two materials, the data together do generally match the MRP-55 trend line as a function of K reasonably well.

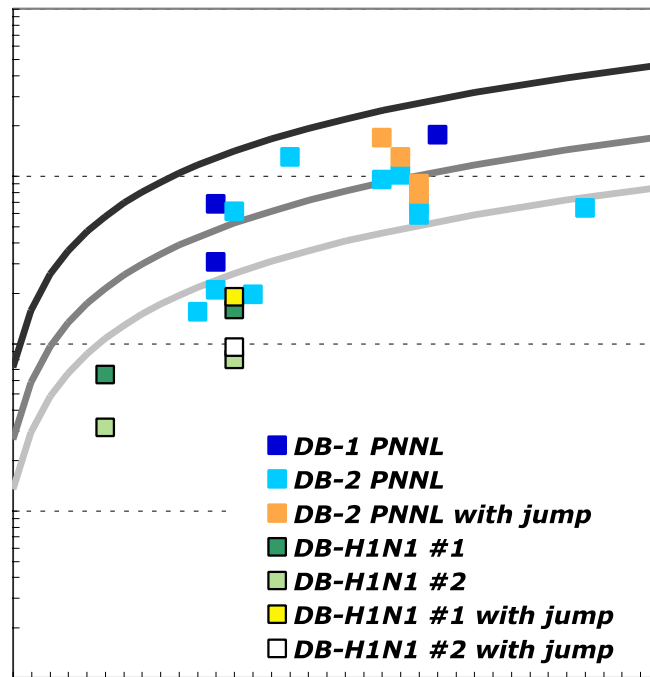


Figure 55. Measured SCC propagation rates versus K for the original Davis Besse head M3935 nozzle (DB-H1N1 #1 and DB-H1N1 #2) and the replacement Davis Besse head M7929 nozzle (DB-1 and DB-2) materials.

Testing on Davis Besse nozzle materials from the original and replacement heads has also been performed at ANL. Two 0.5T CT specimens cut from the original head nozzle #1 (heat 7929) were tested at ANL at 325°C with a dissolved hydrogen content of 23 cc/kg [4]. Microstructural characterization of these materials revealed a small grain size and carbides on grain boundaries similar to that reported here. Measured constant load CGRs for the first test specimen ranged from 5×10^{-9} to 3×10^{-8} mm/s. Subsequent load cycling produced large jumps in crack length suggesting the presence of ligaments, and inclusion of the jumps into the SCC CGRs resulted in values from 1×10^{-8} to 1.3×10^{-7} mm/s for K levels from 23-29 MPa \sqrt{m} . Testing of a second specimen produced constant load propagation rates of 5×10^{-9} to 4×10^{-8} mm/s for K levels ranging from 24-29 MPa \sqrt{m} . An SCC activation energy of 145 kJ/mol was obtained from results at three temperatures, while post-test examination revealed 100% IG engagement. These results are all consistent with those measured by PNNL on adjacent specimens cut from this same nozzle.

Three SCC tests were conducted by ANL at 316°C with 23 cc/kg H₂ on material cut from the Davis Besse replacement head nozzle #3 that was made from heat M3935 [5]. Bulk microstructure characterizations revealed 30-200 μ m size grains, somewhat smaller than observed for the replacement head nozzle #1 reported here. However, high grain boundary carbide coverage was reported for nozzle #3, similar to that found here for nozzle #1. In all SCC tests, 100% IG crack advance took place almost from the start of the tests, however, DCPD-measured crack advance measured on two 0.25T CT specimens provided indeterminate constant load SCC response. For one specimen, growth under constant load was never attained while for the other specimen, no DCPD crack advance was observed except for a nearly instantaneous ~ 40 μ m jump that occurred near the end of the < 200 hour exposure. A constant load crack advance of $\sim 1 \times 10^{-7}$ mm/s was reported for this exposure by including the crack length jump in the SCC propagation rate calculation. A third specimen, this time in a 0.5T CT format, exhibited somewhat more stable constant load crack advance with steady CGRs in the range of 1.3 to 1.6×10^{-7} mm/s for stress intensities ranging from 21-26 MPa \sqrt{m} . These constant load CGRs are 4-5x higher than those reported here at similar K levels but with a distinct difference in dissolved hydrogen and ECP with respect to the Ni/NiO stability line. Taking into account the expected effect of dissolved hydrogen on SCC growth rate for alloy 600, the ANL CGRs are 8-10x higher than those measured by PNNL for the same heat of CRDM material. Besides the difference in corrosion potential, the only other obvious difference is the somewhat smaller grain size reported for nozzle #3. This suggests microstructural differences, perhaps not limited to the grain size, could be responsible for the difference in crack growth rates for the two nozzles.

Summary and Conclusions

Two heats of alloy 600 CRDM tubing from the original and replacement Davis Besse RPV heads were obtained for SCC testing. Microstructural characterizations revealed that the CRDM material from nozzle #1 of the original head (heat M3935) had a very large grain size of ~150-500 μm in diameter and a high density of grain boundary carbides. This suggests that the CRDM nozzle underwent a mill anneal at a temperature sufficient to dissolve all the carbides and was followed a relatively slow cooling rate. The material from nozzle #4 of the replacement head (heat M7929) had a relatively fine grain size of ~10-25 μm in diameter, and carbides were primarily dispersed throughout the material on grain boundaries. This indicates that this CRDM tubing underwent a lower temperature mill anneal where carbides were not dissolved. Both materials were found to have high bulk boron concentrations and extensive boron segregation to grain boundaries. High temperature water exposures of polished coupons of the Davis Besse heats revealed that among other things, boron was selectively removed from grain boundaries ahead of IG oxidation front during corrosion.

SCC testing was performed at 325°C on two 0.25T CT specimens cut from the replacement head nozzle and on two 0.5T CT specimens cut from the original head nozzle. Both materials readily transitioned to 100% intergranular cracking. When taking into account the difference in dissolved hydrogen level for the tests on the two different CRDM materials, the replacement head material appears to have higher SCC susceptibility. Crack growth rates trended along the 75% bounding line of the MRP-55 alloy 600 curve for the small grained replacement head CRDM material where in-service cracking was observed after only ~5.5 years, while the CRDM material from the original head that was in service for ~16 years trended closer to the 50% bounding line.

Crack growth rates reported here for the replacement head nozzle (M7935) are similar to that reported by ANL for testing of this same nozzle. However, the response measured by PNNL for nozzle #1 (M3935) from the original head is distinctly different than that reported by ANL for nozzle #3 (also M3935 from the original head) where reported crack growth rates are ~10x higher when accounting for differences in corrosion potential on crack growth rate. A difference in grain size for nozzle #3 tested by ANL and nozzle #1 tested by PNNL suggest that microstructural differences may be responsible for the apparent difference in SCC susceptibility of the two nozzles. The effect of temperature on constant K crack growth was assessed on the replacement head material with the activation energy for both specimens found to be ~128 kJ/mol. This value is consistent with that measured by ANL. The effect of stress intensity was also assessed and found to reasonably well follow the MRP-55 trendline for the range of K values studied.

References

- [1] D.K. Schreiber, M.J. Olszta, L.E. Thomas, S.M. Bruemmer, "Grain Boundary Characterization of Alloy 600 Prior to and After Corrosion by Atom Probe Tomography and Transmission Electron Microscopy", *Proc. of the 16th International Conference on Environmental Degradation of Materials in Nuclear Power Systems - Water Reactors*, NACE, Asheville, NC, 2013.
- [2] S.A. Attanasio and D.S. Morton, "Measurement of the Nickel/Nickel Oxide Transition in Ni-Cr-Fe Alloys and Updated Data and Correlations to Quantify the Effect of Aqueous Hydrogen on Primary Water SCC", *Proc. of the 11th International Symposium on Environmental Degradation of Materials in Nuclear Power Systems - Water Reactors*, ANS, Stevenson, WA, 2003.
- [3] P.L. Andresen, R. Reid, and J. Wilson, "SCC Mitigation of Ni Alloys and Weld Metals by Optimizing Dissolved H₂", *Proc. of the 14th International Symposium on Environmental Degradation of Materials in Nuclear Power Systems - Water Reactors*, ANS, August, 2009.
- [4] D.S. Dunn, J. Collins, D. Alley, P.G. Oberson, B. Alexandreanu, K. Natesan, S.M. Bruemmer, M.B. Toloczko, "Primary Water Stress Corrosion Cracking Tests and Metallurgical Analyses of Davis-Besse Control Rod Drive Mechanism Nozzle #4", *Proc. of the 16th International Conference on Environmental Degradation of Materials in Nuclear Power Systems - Water Reactors*, NACE, Asheville, NC, 2013.
- [5] B. Alexandreanu, O.K. Chopra, W.J. Shack, "Crack Growth Rates in a PWR Environment of Nickel Alloys from the Davis-Besse and V.C. Summer Power Plants", *NRC NUREG CR-6921*, November 2006.

Acknowledgements

Support for this research is from the Office of Nuclear Regulatory Research, U.S. Nuclear Regulatory Commission (NRC). The views expressed in this paper are not necessary those of the NRC. Helpful interactions with D. Dunn are acknowledged along with the technical assistance of R. J. Seffens, A. D. Guzman and C. E. Chamberlin. Pacific Northwest National Laboratory is operated for the U.S. Department of Energy by Battelle Memorial Institute under Contract DE-AC06-76RLO 1830.